



Multiple stimuli-responsive nanosystem for potent, ROS-amplifying, chemo-sonodynamic antitumor therapy

JunJie Tang^a, Xiaoge Zhang^a, Lili Cheng^a, Yadong Liu^a, You Chen^a, Zhaozhong Jiang^{b, **}, Jie Liu^{a, *}

^a School of Biomedical Engineering, Sun Yat-sen University, Guangzhou, Guangdong, 510006, China

^b Faculty of Arts and Sciences, Department of Biomedical Engineering, Integrated Science and Technology Center, Yale University, 600 West Campus Drive, West Haven, CT, 06516, United States

ARTICLE INFO

Keywords:

Nanoparticle
pH/GSH/ROS triple-Responsive
MRI imaging
Chemodynamic therapy
Sonodynamic therapy

ABSTRACT

Although sonodynamic therapy (SDT) is a promising non-invasive tumor treatment strategy due to its safety, tissue penetration depth and low cost, the hypoxic tumor microenvironment limits its therapeutic effects. Herein, we have designed and developed an oxygen-independent, ROS-amplifying chemo-sonodynamic antitumor therapy based on novel pH/GSH/ROS triple-responsive PEG-PPMDT nanoparticles. The formulated artemether (ART)/Fe₃O₄-loaded PEG-PPMDT NPs can rapidly release drug under the synergistic effect of acidic endoplasmic pH and high intracellular GSH/ROS levels to inhibit cancer cell growth. Besides, the ROS level in the NPs-treated tumor cells is magnified by ART via interactions with both Fe²⁺ ions formed in situ at acidic pH and external ultrasound irradiation, which is not affected by hypoxia tumor microenvironment. Consequently, the enriched intracellular ROS level can cause direct necrosis of ROS-stressed tumor cells and further accelerate the drug release from the ROS-responsive PEG-PPMDT NPs, achieving an incredible antitumor potency. Specifically, upon the chemo-sonodynamic therapy by ART/Fe₃O₄-loaded PEG-PPMDT NPs, all xenotransplants of human hepatocellular carcinoma (HepG2) in nude mice shrank significantly, and 40% of the tumors were completely eliminated. Importantly, the Fe₃O₄ encapsulated in the NPs is an efficient MRI contrast agent and can be used to guide the therapeutic procedures. Further, biosafety analyses show that the PEG-PPMDT NPs possess minimal toxicity to main organs. Thus, our combined chemo-sonodynamic therapeutic method is promising for potent antitumor treatment by controlled release of drug and facile exogenous generation of abundant ROS at target tumor sites.

1. Introduction

Recent anticancer studies show that sonodynamic therapy (SDT) has excellent potential as a ROS-based anticancer treatment with reduced side effects and appreciable drug tolerance [1–6]. Further, SDT is a promising non-invasive treatment strategy for deeply hidden tumors due to the outstanding tissue-penetrating capability of ultrasonic waves [7–11]. Nevertheless, the reactive oxygen species (ROS) generation by sonosensitizer activated with ultrasound at tumor site is oxygen-dependent, thus significantly limited by hypoxia commonly present in typical solid tumors [12–19]. To alleviate the limitation of tumor hypoxia, studies have been carried out to develop

oxygen-enriched system using perfluorocarbon [20,21] and to catalytically produce oxygen in situ in tumor [22,23]. The common feature of all these strategies is that oxygen plays an essential role during the treatment processes. To further amplify the generation of ROS, extensive research has been aimed at designing O₂-independent ROS production system to overcome hypoxia induced SDT resistance [24–28]. For instance, Zhang applied a Ti-TCPP MOF platform to generate ROS in a hypoxic environment and facilitate oxygen-independent SDT treatment [29]. So it would be advantageous to develop oxygen-independent, ROS-generating systems that can conquer SDT resistance induced by hypoxia [30].

Artemisinin extracted from *Artemisia annua* is an important

Peer review under responsibility of KeAi Communications Co., Ltd.

* Corresponding author.

** Corresponding author.

E-mail addresses: zhaozhong.jiang@yale.edu (Z. Jiang), liujie56@mail.sysu.edu.cn (J. Liu).

<https://doi.org/10.1016/j.bioactmat.2021.12.002>

Received 3 September 2021; Received in revised form 19 November 2021; Accepted 6 December 2021

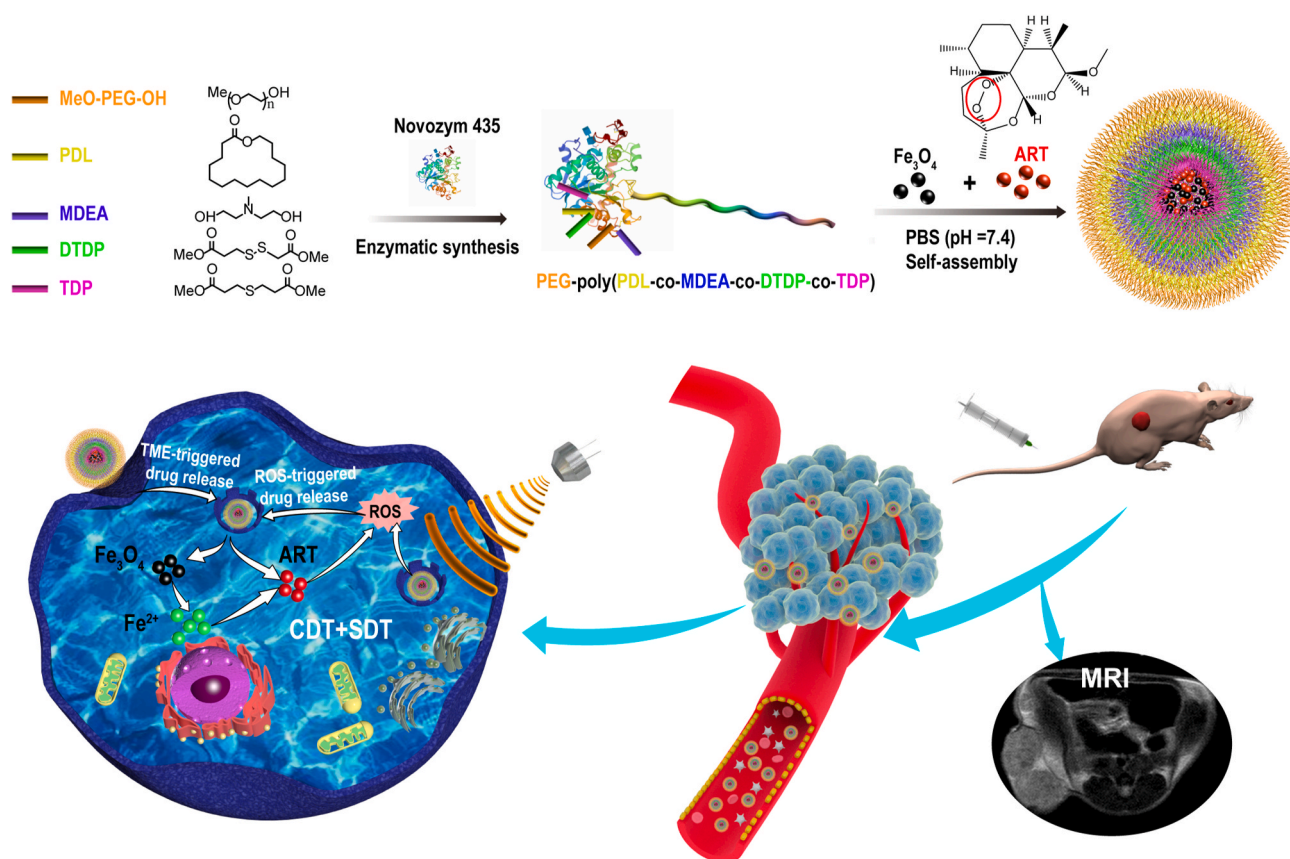
Available online 20 December 2021

2452-199X/© 2022 The Authors. Publishing services by Elsevier B.V. on behalf of KeAi Communications Co. Ltd. This is an open access article under the CC BY-NC-ND license (<http://creativecommons.org/licenses/by-nc-nd/4.0/>).

antimalarial drug and has also been shown to possess antitumor properties [31–34]. Artemisinin derivatives exert antitumor activities by influencing the growth, apoptosis, proliferation and metastasis of tumor cells [35–37]. These drugs containing endoperoxide groups are cytotoxic to tumor cells through complex interactions involving different signaling pathways [38,39]. Further, in addition to serve as chemotherapeutic drugs, artemisinin derivatives can be used to generate ROS in a sonodynamic therapy via interaction with ultrasound irradiation to break their bridging endoperoxide bonds (R-O-O-R') or in a chemodynamic therapy (CDT) via interaction with intracellular Fe^{2+} ions [40–43]. Artemether (ART) is a typical artemisinin derivative that exhibits good anticancer therapeutic potential and is capable of generating ROS upon ultrasonication without oxygen [32,39]. Wang applied core-shell structured nanoparticles to encapsulate artemisinin and ultrasound (1 MHz, $2\text{W}/\text{cm}^2$) was employed to realize drug procedural controlled release and cancer sonodynamic combined therapy [42]. ART kills tumor cells by promoting protein alkylation and blocking cell cycle [44–46]. The use of ART as an oxygen-independent sonosensitizer for ROS production would eliminate the oxygen-deficient problem for SDT in hypoxic tumor environments. Thus, we hypothesize that it is feasible to develop efficient combined CDT and SDT using ART as a dual-functional therapeutic agent.

To achieve controlled release delivery of hydrophobic drug ART in tumor site, we designed and constructed novel nanoparticles from enzymatic PEG-poly(ω -pentadecalactone-co-N-methyl-diethyleneamine-co-3,3'-dithiodipropionate-co-3,3'-thiodipropionate) copolymers (PEG-PPMDT), which are biodegradable and can respond to tumor microenvironments. We have previously reported that poly(ethylene glycol)-poly(ω -pentadecalactone-co-N-methyl-diethyleneamine-co-sebacate) (PEG-PPMS) and poly(ethylene glycol)-poly(ω -pentadecalactone-co-N-methyl-diethyleneamine-co-3,3'-thiodipropionate) (PEG-PPMT) block

copolymers are responsive to tumor-relevant acidic pH and pH/ROS in tumor matrix, respectively [47,48]. In comparison, the newly synthesized PEG-PPMDT polymers in this study contain tertiary amino, disulfide and thioether functional groups in the main chain, which are responsive to acidic endoplasmic pH and highly elevated ROS/GSH (glutathione) levels in tumor cells. We successfully transformed PEG-PPMDT via self-assembly processes to pH/ROS/GSH triple-responsive nanoparticles, loaded the NPs with ART and Fe_3O_4 , and comprehensively evaluated the properties and antitumor efficacy of the ART/ Fe_3O_4 -loaded NPs under various pH and ultrasonication conditions *in vitro* and *in vivo*. The design rationales for constructing the current drug nanocarriers for desirable chemo-sonodynamic therapy are based on following assumptions: (i) the PEGylated NPs have prolonged blood circulation time and can efficiently concentrate in tumor via the EPR effect [49]; (ii) after internalization by tumor cells, the drug encapsulated in PEG-PPMDT NPs can be released rapidly under the synergistic effect of acidic endoplasmic pH and high intracellular GSH/ROS levels to achieve rapid killing of the cells [50–52]; (iii) amplified ROS generation via interactions of ART with free Fe^{2+} ions released from Fe_3O_4 at acidic pH and with external ultrasound irradiation would further accelerate the drug release and induce direct killing of ROS-stressed tumor cells, thus yielding an extraordinary antitumor potency [53,54]; (iv) Fe_3O_4 encapsulated in the NPs can additionally serve as an efficient MRI contrast agent to guide the therapeutic procedures [55,56]. Scheme 1 elucidates the hypothetical pathway of ART/ Fe_3O_4 -loaded PEG-PPMDT NPs for tumor microenvironment pH/ROS/GSH triple-responsive drug release and antitumor therapy with enhanced efficiency under controllable external ultrasonication.



Scheme 1. Hypothetic action path of ART/ Fe_3O_4 -loaded PEG-PPMDT NPs for tumor microenvironment triple-responsive drug delivery at tumor site with efficiency further enhanced by external ultrasonication.

2. Experimental section

2.1. Materials, cell culture and animals

Poly(ethylene glycol) methyl ether (MeO-PEG2K-OH, 2000 Da), dimethyl 3,3'-thiodipropionate (TDP), dimethyl 3,3'-dithiodipropionate (DTDP), ω -pentadecalactone (PDL), *N*-methyl diethanolamine (MDEA) and Novozym 435 (immobilized *Candida antarctica* lipase B in acrylic resin) were purchased from Aldrich Chemical Co. Artemether (ART), coumarin 6 (C6), Cyanine 5.5 (Cy5.5), Hoechst 33342 and MTT were acquired from Sigma. Fe₃O₄ NPs were acquired from Nanjing Nanoeast Biotech Co., Ltd. HepG2 tumor cells were provided by Shanghai Cell Bank of the Chinese Academy of Sciences (Shanghai, China) and cultured with DMEM (Hyclone). Male nude BALB/c mice were obtained and raised in the Center for Experimental Animals at Sun Yat-sen University. To obtain xenograft HepG2 tumor-bearing mice, approximately 1×10^7 HepG2 cells were subcutaneously inoculated into the lateral abdomen of the mice. All animal experiments were approved by the Animal Care and Use Committee of Sun Yat-sen University. During antitumor experiments *in vivo*, the tumor volume was measured via vernier caliper and calculated by the following equation:

$$\text{Volume} = 0.5 \times \text{length} \times (\text{width})^2$$

2.2. Procedures for the synthesis of PEG-poly (PDL-co-MDEA-co-DTDP-co-TDP) (PEG-PPMDT) copolymers

Reaction substrates consisting of MeO-PEG2K-OH, dimethyl 3,3'-dithiodipropionate (DTDP), dimethyl 3,3'-thiodipropionate (TDP), *N*-methyl diethanolamine (MDEA), and ω -pentadecalactone (PDL), were dissolved in 200 wt% diphenyl ether vs total substrate and polymerized in the presence of 10 wt% Novozym 435 vs total substrate. The reaction mixtures were heated at 90 °C under 1 atm nitrogen pressure for 22 h, then under a reduced pressure of 1.8 mmHg for 70 h. After the reactions were completed, the formed polymer products were purified by the following procedures. Firstly, an excess of *n*-hexane was added into the product mixtures to precipitate the resultant polymers, followed by washing the polymer products twice with *n*-hexane. After dissolution of the polymers in chloroform and subsequent filtration to remove the catalyst particles, the polymer solutions were concentrated by vacuum and added dropwise to agitated *n*-hexane to reprecipitate the polymer products. The purified polymers were vacuum-dried at 30 °C for 24 h. The different substrate ratios used for synthesizing the polymers are listed in Table 1.

PEG-PPMDT block copolymers: ¹H NMR (CDCl₃; ppm) 1.26 (br.), 1.62 (m), 2.31 (t), 2.35 (s), 2.63 (t), 2.72 (t), 2.75 (t), 2.80 (t), 2.92 (t), 3.64 (s), 4.08 (t), 4.19 (t/br.); ¹³C NMR (CDCl₃; ppm) 24.91, 25.88, 26.93, 28.57, 29.13, 29.23, 29.27, 29.46–29.62 (m), 33.00, 34.04, 34.26, 34.68, 42.83, 55.83, 62.35, 62.42, 64.91, 64.98, 70.54, 171.57, 171.70, 173.75.

Table 1
Characterization of PEG-PPMDT copolymers.

sample ^a	PDL/DTDP/TDP/MDEA/PEG2K (feed molar ratio)	isolated yield	TDP Content (mol%) ^b	M _w (Da) ^c	M _w /M _n ^c
PEG-PPMDT1	11.1:90:10:95:10	82%	13%	13600	1.7
PEG-PPMDT2	11.1:70:30:95:10	82%	34%	14100	1.8
PEG-PPMDT3	11.1:50:50:95:10	80%	52%	12900	1.8
PEG-PPMDT4	11.1:30:70:95:10	75%	71%	12900	1.8
PEG-PPMDT5	11.1:10:90:95:10	78%	89%	12100	1.7

^a All block copolymers contain (40 ± 1) wt% PEG and (11 ± 1) mol% PDL units vs (PDL + diester) units.

^b Mol% TDP units vs (TDP + DTDP) units in the copolymer chains.

^c Measured by gel permeation chromatography (GPC) via narrowly polydisperse polystyrene standards.

2.3. Fabrication and characterization of pH, GSH and ROS triple-responsive PEG-PPMDT nanoparticles

Amphiphilic PEG-PPMDT copolymers were used to form nanoparticles through self-assembly in aqueous phase. Briefly, PEG-PPMDT copolymer (25 mg) was dissolved in 0.5 mL THF, dropwise injected to 2.5 mL PBS (10 mM, pH = 7.4), and stirred for 30 min at 25 °C. The solution was subsequently dialyzed (with 7000 Da cutoff size) in PBS-pH 7.4 overnight. The preparation of ART/Fe₃O₄-loaded PEG-PPMDT NPs was similar to blank PEG-PPMDT NPs, a mixture of 2 mg ART and 0.2 mg Fe₃O₄ nanoparticles was also co-dissolved. ART-loaded PEG-PPMDT NPs were fabricated analogously without using Fe₃O₄ nanoparticles. Zetasizer Nano ZS90 (Malvern Instruments) and transmission electron microscope (TEM, Hitachi H-7650) were employed to analyze the size distribution and morphology of PEG-PPMDT NPs.

High Performance Liquid Chromatography (HPLC, Shimadzu LC-2030) was employed for determining the drug loading (DL) and entrapment efficiency (EE) of ART in PEG-PPMDT NPs. To prepare samples for analysis, the nanoparticle solution was dissolved in excessive THF, centrifuged (13000 rpm, 10 min) and filtered by membrane syringe (0.22 μm). The amount of ART was measured using a UV detector at 210 nm (mobile phase: 70:30 acetonitrile/water). The following formulas were used to calculate the DL% and EE%:

$$\text{DL}\% = \frac{\text{drug amount in nanoparticles}}{\text{mass of nanoparticles}} \times 100\%$$

$$\text{EE}\% = \frac{\text{drug amount in nanoparticles}}{\text{amount of drug feed}} \times 100\%$$

The content of Fe₃O₄ in the micelles was determined by inductively coupled plasma-atomic emission spectrometry (ICP-AES). The Fe₃O₄-loaded PEG-PPMDT nanoparticle solution was added into concentrated nitric acid to allow nitration for 24 h until the solution is colorless. After filtration of the reaction mixture by a membrane syringe (0.22 μm), the sample was analyzed by ICP-AES. The loading density of Fe₃O₄ was calculated by the weight ratio of Fe₃O₄ over the PEG-PPMDT micelle.

2.4. pH, GSH and ROS triple-responsive properties of PEG-PPMDT NPs

The drug release behavior of ART-loaded PEG-PPMDT NPs was explored under different pH (7.4, 6.5) and redox (0–100 μM H₂O₂ and/or 0–10 mM GSH) conditions at 37 °C. Briefly, ART-loaded PEG-PPMDT NPs (PA NPs) and ART/Fe₃O₄-loaded PEG-PPMDT NPs (PAF NPs) were dialyzed in PBS with various pH and redox levels, and the profiles of ART release from PEG-PPMDT NPs were determined by HPLC. During the processes, the particle size distribution and morphology of the NPs were monitored through DLS and TEM. To study the effects of ultrasound-induced ROS formation on drug release behavior of the PEG-PPMDT NPs, varied ultrasonication conditions were used (1–3 W/cm² irradiation intensity, duration for 10 min or 30 s every 30 min).

2.5. ROS generation in solution

1,3-Diphenylisobenzofuran (DPBF) was employed to assay ROS

formation by ART from PEG-PPMDT micelles in PBS solution. To analyze ROS generated by artemether under ultrasound irradiation, 2 mL PBS solution containing free ART (or ART-loaded PEG-PPMDT NPs) and 10 mM DPBF was treated by ultrasound (1 MHz, 2 W/cm²) for varied time, and the absorbance of DPBF was monitored by UV detector at 413 nm. Further, PAF NPs were incubated with PBS solutions of different pH for various time lengths, and ROS production was also determined by DPBF to verify the self-promoted ROS-generation activity of the NPs.

2.6. *In vitro* imaging properties of ART/Fe₃O₄-loaded PEG-PPMDT NPs

A series of ART/Fe₃O₄-loaded PEG-PPMDT solutions in PBS were prepared for magnetic resonance imaging (MRI) *in vitro*. Briefly, solutions of PAF NPs (100 μL) with different Fe₃O₄ concentrations were added into 48 orifice and scanned by clinical 1.5-T MRI system Achieva (Philips Medical Systems, Best, the Netherlands). The value of T₂ relaxation time was measured to obtain a linear plot of R₂ relaxation rate (1/T₂) vs the NPs concentration.

2.7. Cellular experiments

2.7.1. Cellular uptake

To study cellular uptake, coumarin-6 (C6) was encapsulated in PEG-PPMDT micelles by the method similar to the one for preparing blank PEG-PPMDT micelles, except that a mixture of C6 and PEG-PPMDT was used instead of the polymer alone. HepG2 cells (3 × 10⁵ cells/mL) were seeded into 6-well culture plates for overnight incubation. After reaching a confluence of 70%, the adherent cells were treated with fresh DMEM medium containing C6-loaded PEG-PPMDT NPs or free C6 at 0.2 μg/mL C6 concentration for 1–8 h. Subsequently, the HepG2 cells were collected by trypsinization, centrifuged and washed by PBS. The fluorescence intensity of C6 in single cell suspension was measured by flow cytometry (Becton Dickinson, San Jose).

The intracellular distribution of C6-loaded PEG-PPMDT NPs was observed by confocal laser scanning microscopy (CLSM) (TCS sp5). Briefly, HepG2 cells (1 × 10⁵ cells/mL) were seeded on confocal bottom dishes and treated with C6-loaded PEG-PPMDT NPs or free C6 (control) at 0.2 μg/mL C6 concentration for 6 h. Thereafter, the HepG2 cells were stained by Hoechst 33342 and LysoTracker Red DND-99, and visualized through CLSM. The excitation wavelengths of Hoechst 33342, LysoTracker Red DND-99 and C6 were 405 nm, 577 nm and 467 nm, respectively.

2.7.2. Cellular ROS generation

To investigate intracellular ROS production, HepG2 cells (1 × 10⁵ cells/mL) were plated at 6-well culture plates and confocal bottom dishes for overnight incubation. Thereafter, the adherent cells were randomly divided into 9 groups as control, pH 7.4 PA NPs, pH 7.4 PA NPs (+), pH 6.5 PA NPs, pH 6.5 PA NPs (+), pH 7.4 PAF NPs, pH 7.4 PAF NPs (+), pH 6.5 PAF NPs and pH 6.5 PAF NPs (+) groups [(+) represents additional ultrasound irradiation treatment (1 MHz, 2 W/cm², 3 min)]. After the HepG2 cell groups were incubated under their respective treatment conditions for 6 h (ART concentration = 40 μg/mL for all groups), the culture medium was replaced with 20 μM DCFH-DA to react with intracellular ROS for 20 min. Subsequently, the DCF fluorescence intensity of all groups in single cell suspension was quantitatively measured by flow cytometry and observed under CLSM. The fluorescent dye Hoechst 33342 and DCF were excited at 405 nm and 488 nm, respectively.

2.7.3. Cytotoxicity

MTT assay was used for cytotoxicity evaluation. Briefly, HepG2 cells (5000 cells/well) were seeded in 96-well plates for overnight incubation, and the cells in each well were treated for 6 h by different drug formulations with ART concentration ranging from 1.25 to 160 μg/mL.

Thereafter, the culture medium with NPs was replaced by fresh DMEM medium, and the treated cells were irradiated by ultrasound (1 MHz, 2 W/cm²) for 3 min. After the ultrasound treatment, 120 μL fresh medium with 20 μL MTT (5 mg/mL) was incubated with the cells in each well for 4 h. Finally, the formed formazan salt crystals were dissolved in DMSO and assayed by microplate reader (BioTek Synergy 4). The following formula was employed to calculate the relative cell viability (%):

$$\text{Cell viability (\%)} = \frac{A_{\text{sample}} - A_{\text{blank}}}{A_{\text{control}} - A_{\text{blank}}} \times 100\%$$

where A_{blank} is the cell-free absorbance at 570 nm, and A_{control} and A_{sample} are the absorbance values obtained from the sample without NPs and the sample with NPs, respectively.

2.7.4. Cell apoptosis

To investigate apoptosis induced by the ART/Fe₃O₄-loaded NPs, HepG2 cells (3 × 10⁵ cells/mL) were plated at 6-well plates for overnight adhesion. Thereafter, the adherent cells were incubated with various formulations with 40 μg/mL ART for 6 h. Selected cells (US groups) were additionally irradiated by ultrasound (1 MHz, 2 W/cm², 3 min). Upon 24 h incubation, the HepG2 cells were collected by trypsinization, centrifuged and washed by PBS. Subsequently, the collected cells were stained with 5 μL AnnexinV-FITC and 5 μL propidium iodide (PI) for 15 min in the absence of light, and analyzed with flow cytometry.

2.7.5. Cell cycle

The method of cell cycle analysis was similar to the apoptosis assay above. HepG2 cells (3 × 10⁵ cells/mL) were seeded and treated according to the same procedure for cell apoptosis study. At last, the HepG2 cells were resuspended in PBS, stained with PI for 30 min in the absence of light, and then analyzed with flow cytometry.

2.8. Animal experiments

2.8.1. *In vivo* magnetic resonance imaging

The subcutaneous tumor model of HepG2 was established by subcutaneously inoculating 1 × 10⁷ HepG2 cells to the lateral abdomen of the mice. The experiments were carried out when the tumor volume increased to 100 mm³. After ART/Fe₃O₄-loaded PEG-PPMDT NPs (200 μg/mL) were injected intravenously into the tumor-bearing nude mice and aggregated to the tumor site through the EPR effect, the MRI signals of the tumors were analyzed by clinical 1.0-T MRI system (Aspect M3, Aspect Imaging) with linear polarization bird cage RF rat coil. The specific detection parameters of tumor region axial T₂ weighted images were as follows: TR = 3750 ms, TE = 95 ms, slice thickness = 2 mm, slice number = 11.

2.8.2. Biodistribution

The distribution of PEG-PPMDT NPs *in vivo* was studied by small animal imaging system (IVIS® Lumina XR Series III, PerkinElmer), and Cy5.5 was used as a fluorescent marker. The tumor model was constructed as described in section 2.8.1. Cy5.5-loaded PEG-PPMDT NPs and free Cy5.5 were injected intravenously to tumor-bearing nude mice at Cy5.5 concentration of 0.4 mg/kg. The fluorescence signals of the mice were recorded by the imaging system from 1 h to 24 h after injection. The mice were dissected, and their tumors and normal organs were collected after 24 h. The fluorescence intensity of each organ was detected and quantified by *ex vivo* imaging.

2.8.3. *In vivo* antitumor activity

To study antitumor activity *in vivo*, the tumor-bearing mice with tumor volume reaching approximately 100 mm³ were randomly divided into six groups (n = 5): (i) 0.9% NaCl (control), (ii) free ART, (iii) PA NPs, (iv) PA NPs (+), (v) PAF NPs, (vi) PAF NPs (+). The sign (+) represents additional ultrasound irradiation treatment (1 MHz, 2 W/cm²,

10 min) after 8 h post-injection. Different drug formulations with 20 mg/kg ART and 1 mg/kg Fe₃O₄ (in case of PAF NPs) were injected intravenously to the mice on Day 0, 3, and 6, respectively. The body weight and tumor volume changes of the mice were recorded every two days throughout the treatment. The Kaplan-Meier survival curves were obtained by the percent mice when the tumor volume >1000 mm³ or the mice died. On the 22nd day, tumors and main organs were harvested from the mice, weighed and photographed. The tumor suppression effect of ART/Fe₃O₄-loaded PEG-PPMDT micelles was evaluated by analyzing the results of hematoxylin and eosin (H&E) and TUNEL staining.

2.8.4. Biosafety

To evaluate possible side effects of ART/Fe₃O₄-loaded PEG-PPMDT NPs, the main organs of treated mice were excised at the end of anti-tumor experiments, stained by H&E for toxicity test of the NPs. Additionally, blood samples were collected by eye puncture for analysis on levels of alkaline phosphatase (ALP), alanine aminotransferase (ALT), aspartate transaminase (AST), creatinine (CRE), urea nitrogen (BUN) and creatine kinase (CK).

2.9. Statistical analysis

All experiments were repeated three times at least to obtain means ± standard deviation. The experimental results were analyzed by *t*-test and considered as statistically significant at **p* < 0.05, ***p* < 0.01 and ****p* < 0.001.

3. Results and discussion

3.1. Synthesis and characterization of PEG-PPMDT block copolymers

PDL, DTDP, TDP, MDEA and MeO-PEG2K-OH were copolymerized with Novozym 435 catalyst to produce PEG-PPMDT block copolymers (Scheme 2). The composition of the copolymers was controlled by the ratio of the monomers. The yield of the synthesized polymers was 75–82%, and their molecular weights (*M_w*) ranged from 12100 to 14100 Da with a polydispersity of 1.7–1.8 (Table 1).

During the polymer syntheses, PDL and PEG in specific amounts were

used to ensure that the final formed block copolymers contain approximately 40 wt% PEG and 10 mol% PDL (Table 1). Our previous results indicate that micelles composed of PEG-poly(amine-co-ester) block copolymers have high colloidal stability at 40 wt% PEG, and a PDL content at ~10 mol% can effectively promote cellular uptake of such micelle nanoparticles [48]. The DTDP/TDP unit ratio can be easily adjusted by using different amounts of DTDP and TDP in the monomer feeds (Table 1). Because MeO-PEG2K-OH can only connect to the terminal of PPMDT chains, the PEG-PPMDT copolymers have two possible chain structures including PEG-PPMDT diblock chain and PEG-PPMDT-PEG triblock chain (Scheme 2).

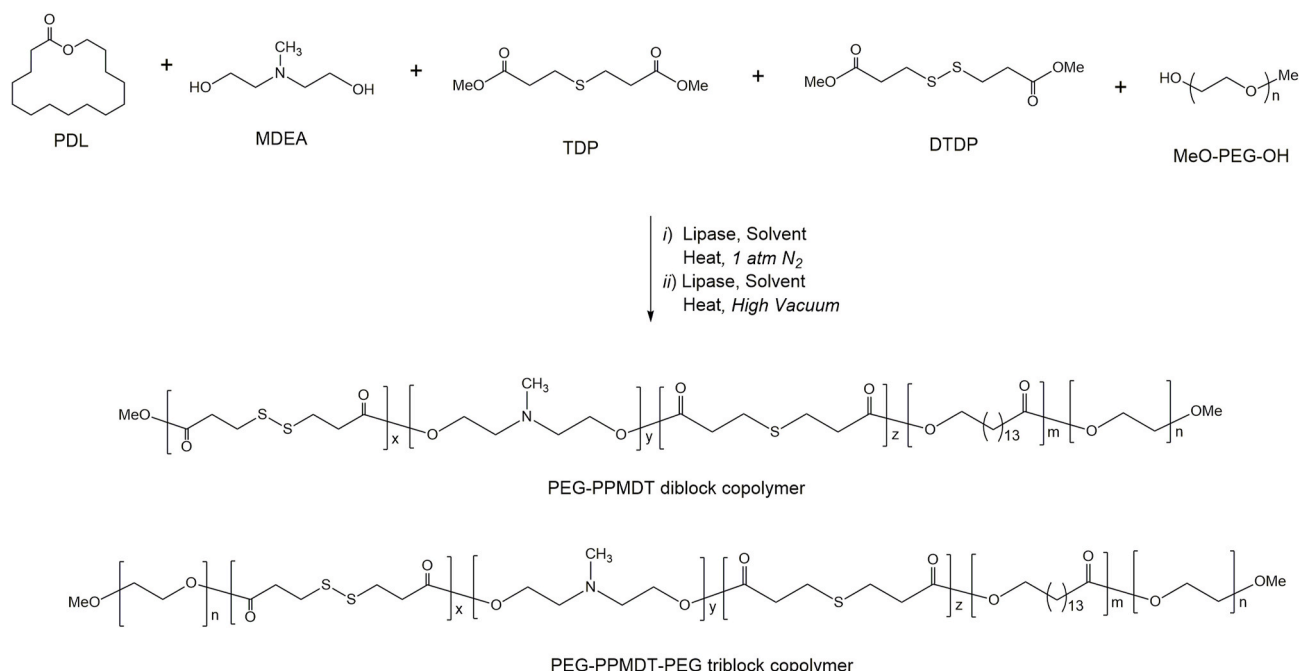
The molecular structure of PEG-PPMDT copolymers was confirmed by both proton and carbon-13 NMR spectroscopy. The detailed analyses on ¹H and major ¹³C resonance absorbances of the polymers are described in supporting information (Fig. S1). By comparing the integrated proton absorption intensities of different repeat units in the polymer chains, the polymer compositions were determined (Table 1).

3.2. Fabrication and characterization of PEG-PPMDT nanoparticles

Micelle nanoparticles of amphiphilic PEG-PPMDT copolymers were prepared by self-assembly processes and purified by dialysis. As shown in Table 2, the average diameter of ART/Fe₃O₄-loaded PEG-PPMDT NP

Table 2
Characterization data of ART/Fe₃O₄-loaded PEG-PPMDT micelles.

Copolymer	Size (nm)	PDI	ζ (mV)	Fe ₃ O ₄ loading (%)	ART	
					DL (%)	EE (%)
PEG-PPMDT1	148.2 ± 3.4	0.144 ± 0.05	-2.1 ± 0.5	15.15 ± 1.2	3.00 ± 0.2	63.0 ± 2.5
PEG-PPMDT2	149.1 ± 2.1	0.121 ± 0.03	-2.3 ± 0.7	14.65 ± 0.7	3.02 ± 0.2	62.7 ± 4.2
PEG-PPMDT3	148.4 ± 3.1	0.042 ± 0.01	-2.2 ± 0.5	15.32 ± 1.1	3.01 ± 0.1	63.2 ± 2.8
PEG-PPMDT4	161.1 ± 1.3	0.091 ± 0.04	-2.1 ± 0.8	14.15 ± 0.6	3.32 ± 0.2	69.9 ± 3.5
PEG-PPMDT5	156.2 ± 2.2	0.112 ± 0.03	-2.8 ± 0.3	14.75 ± 0.8	3.21 ± 0.4	65.4 ± 5.2



Scheme 2. Enzymatic synthesis of PEG-PPMDT block copolymers.

samples range from 148 to 161 nm, which is conducive for the NPs to avoid RES clearance and aggregate into tumor sites through the EPR effect. HPLC analysis revealed that the ART/ Fe_3O_4 -loaded PEG-PPMDT NP samples contained 3.0–3.3% drug and the drug entrapment efficiency was 63–70% during the NP fabrications (Table 2). All NP samples are negatively charged on the surface, which can minimize their binding with serum protein to prolong blood circulation time, thus enhancing their drug delivery efficiency *in vivo*.

Transmission electron microscopy (TEM) further revealed the sizes and spherical structure of the drug-loaded PEG-PPMDT NPs. As shown in Fig. 1A and B, the ART-loaded PEG-PPMDT3 (PA) NPs possessed an average diameter of 150 nm, and the average size of ART/ Fe_3O_4 -loaded PEG-PPMDT3 (PAF) NPs was about 10 nm larger due to the addition of Fe_3O_4 NPs (15% loading). The internal Fe_3O_4 nanoparticles were observed in the TEM images of PAF NPs (Fig. 1B). Importantly, the PEG-PPMDT NPs possessed low CMC values (Table S1 and Fig. S2) and high stability in PBS containing 10% FBS for 7 days (Fig. S3).

3.3. Tumor microenvironment-responsive properties of PEG-PPMDT nanoparticles

PEG-PPMDT polymer chains contain tertiary amino, thioether and disulfide functional groups, which are responsive to acidic pH, elevated ROS (e.g., H_2O_2) and GSH levels, respectively. To investigate stimuli-responsive capability of PEG-PPMDT NPs, we used ART-loaded PEG-PPMDT3 NPs as a typical example for study on their property changes under various tumor-mimicking microenvironments. In the media with mild acidic pH of 6.5 (Fig. 1C) or elevated H_2O_2 level (Fig. 1D), the size of the NPs gradually increased as a result of the protonation of tertiary

amino groups and partial oxidation of thioether moieties in the polymer, transforming the hydrophobic cores of the NPs to be hydrophilic. Upon incubation of the NPs in PBS containing 10 mM GSH, the average size of the NPs rather decreased due to disulfide bond reduction and polymer chain cleavage. The new micelles containing the lower molecular weight block copolymers would have a smaller size (Fig. 1E). In a tumor-mimicking acidic medium with high concentrations of H_2O_2 and GSH, multiple reactions would occur simultaneously in the micelles to form nanoparticles with a bimodal size distribution: large NPs resulted from the amino protonation and thioether oxidation, and smaller NPs formed by the reductive cleavage of disulfide bonds (Fig. 1F). Compare to slight size changes under single tumor-mimicking condition, the PEG-PPMDT NPs would undergo multiple changes in the conditions simulating the tumor-mimicking microenvironment. Because under the promotion of a single external condition, the hydrophilic transformation or chain fracture of the hydrophobic polymer segment in the nanoparticles is limited, which induced slightly size changes of PEG-PPMDT NPs. And when multiple stimuli conditions exist, the disulfide bond of PEG-PPMDT would cleave in the presence of GSH, which reduced the hydrophobic property of the copolymer. After further hydrophilic transformation by pH and ROS response, the amphiphilic structure of the polymer increased significantly, resulting in serious changes in the morphology of nanoparticles. We have further examined the morphology and size distribution of nanoparticles in lower pH value and high redox levels in Fig. S4, more obvious swelling phenomenon could be observed under the conditions of pH 5.0 and 200 μM H_2O_2 . Moreover, the structural cracking of PEG-PPMDT NPs would become more obvious due to the disulfide bond cleavage at higher GSH concentration. Importantly, as demonstrated below, all these tumor-relevant chemical

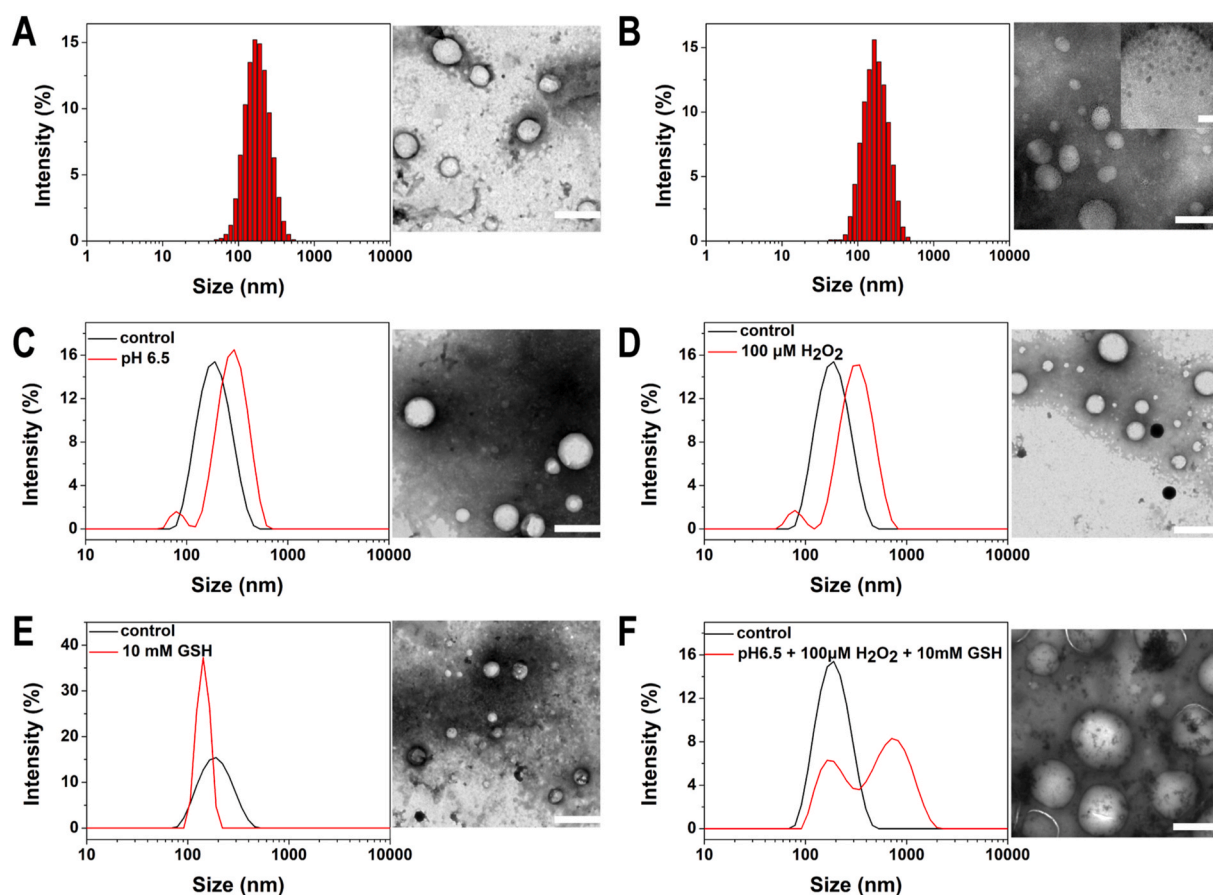


Fig. 1. TEM analyses of ART-loaded PEG-PPMDT (PA) NPs (A) and ART/ Fe_3O_4 -loaded PEG-PPMDT (PAF) NPs (B), and size distribution and TEM images of PA NPs incubated with PBS-pH 6.5 (C), 100 μM H_2O_2 (D), 10 mM GSH (E) and PBS-pH 6.5 + 100 μM H_2O_2 + 10 mM GSH (F) for 24 h. Scale bar = 200 nm in (A)–(F), scale bar = 20 nm in the inset of (B).

reactions (amino protonation, thioether oxidation and disulfide reduction) promote drug release from the NPs since the reactions yield highly swollen micelles with more hydrophilic cores.

The drug release kinetics of ART-loaded PEG-PPMDT micelles were studied under normal physiological conditions and tumor-mimicking environments. As depicted in Fig. 2A and B, the accumulative drug release of ART-loaded PEG-PPMDT3 (PA) NPs and ART/ Fe_3O_4 -loaded PEG-PPMDT3 (PAF) NPs was relatively slow in pH 7.4 PBS. The drug release rates significantly increase when the medium pH is decreased to 6.5, or when H_2O_2 (100 μM) or GSH (10 mM) is added to the medium. The highest cumulative drug release values (>80%) at ≥ 24 h were observed in acidic PBS (pH 6.5) containing both H_2O_2 (100 μM) and GSH (10 mM). As shown in Fig. S5-A&B, the PA NPs and PAF NPs showed gradient drug release with the increase of acidity and redox level. Additionally, Fe_3O_4 tend to decompose in acidic media to form free Fe^{2+} ions, which can cleave the bridging peroxide bond of ART to generate more ROS. Therefore, the PAF NPs had better pH responsiveness than PA NPs as the resultant ROS from PAF NPs would accelerate the drug

release in lower pH values. Additional supporting data on the drug release ability of other PEG-PPMDT NPs are also presented in Figs. S5-D, E, F. These results demonstrate the synergistic, multiple stimuli-responsive properties of multifunctional PEG-PPMDT copolymers, and are consistent with the inherent repeat unit structures of the polymer chains which can absorb protons and react with H_2O_2 /GSH to form disintegrated micelle cores with highly hydrophilic ammonium cations, sulfoxide/sulfone groups and thiol moieties. Consequently, PEG-PPMDT NPs can be triggered in PBS mimicking tumor microenvironment to rapidly release the encapsulated drug to the media.

Compared to PA NPs, PAF NPs possess not only additional MRI imaging capability (to be discussed in a latter section) but also ability to self-produce ROS in acidic tumor environments or acidic endosomes/lysosomes of cancer cells. Fe_3O_4 tends to decompose in acidic media to form free Fe^{2+} ions which can cleave the bridging peroxide bond of ART to generate potent ROS (to be discussed in a latter section). The resultant ROS would accelerate the drug release from PAF NPs or directly kill tumor cells, thus remarkably promoting the antitumor efficacy of the

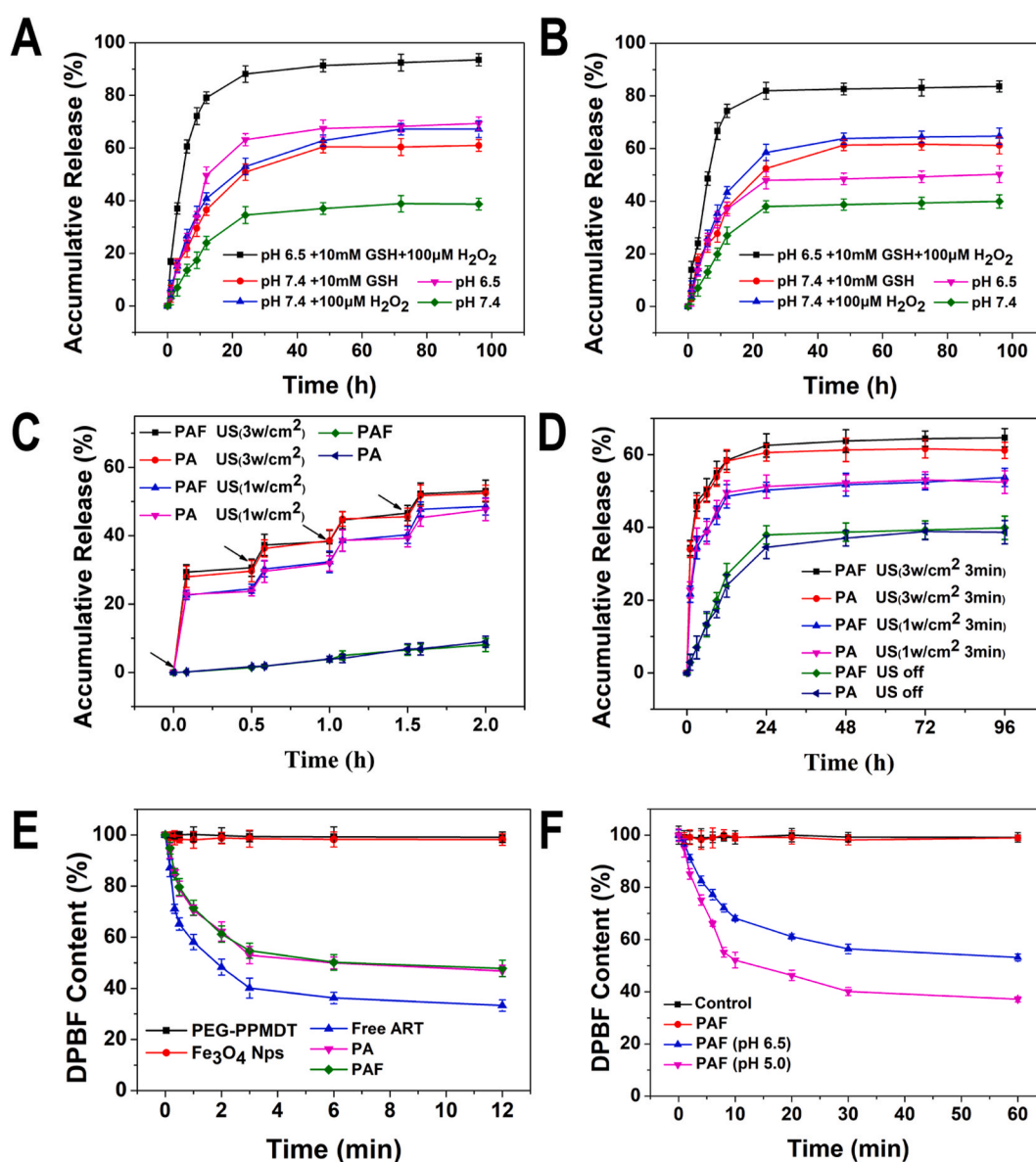


Fig. 2. Accumulative drug release profiles of ART/ Fe_3O_4 -loaded PEG-PPMDT3 (PAF) NPs (A) and ART-loaded PEG-PPMDT3 (PA) NPs (B) under acidic and/or redox conditions. Drug release curves of the NPs in pH 7.4 PBS either with intermittent on/off ultrasound for 30 s every 30 min (C) or with irradiation by different intensity ultrasound (D). The changes of DPBF absorbance at 413 nm vs duration with ultrasound irradiation (1 MHz, 2 W/cm²) on the solution of DPBF/NPs mixture in PBS with pH 7.4 (E), and changes of DPBF absorbance value for DPBF/PAF NPs solutions in PBS with varied pH (F).

NPs. Consistent with this hypothesis, at 96 h in PBS (pH 6.5) containing both H₂O₂ (100 μM) and GSH (10 mM), PAF NPs had a significantly higher cumulative drug release value (93.5%) than PA NPs (81%) (Fig. 2A&B). In contrast, both PAF NPs and PA NPs exhibited comparable, much lower drug release rates in pH 7.4 PBS. These experimental data indicate that PAF NPs can remain fairly stable during blood circulation, and respond to acidic endosomal pH and elevated intracellular ROS/GSH levels to achieve rapid drug release for enhanced cytotoxicity. The outstanding anticancer efficacy of PAF NPs will be demonstrated in subsequent sections.

3.4. *In vitro* ultrasound-accelerated drug release

ART can serve not only as a chemotherapeutic agent for antitumor treatment, but also as a sonosensitizer (responsive to 1 MHz ultrasound irradiation) to accelerate the drug release from PEG-PPMDT NPs. As shown in Fig. 2C, under intermittent 3-min ultrasound irradiation (1 MHz, 1 or 3 W/cm²) every 0.5 h, the cumulative drug release from PA NPs and PAF NPs in pH 7.4 PBS jumped after every irradiation, indicating that the drug release behavior can be accurately controlled by external ultrasound. Except for the duration and frequency of ultrasound irradiation, the intensity of ultrasound also has a significant effect on drug release. For instance, the accumulative drug release from PA NPs increased from 38.6% to 53.7% at 96 h upon 1 W/cm² ultrasonication (1 MHz, 3 min), and further up to 64.6% with 3 W/cm² ultrasonication (1 MHz, 3 min) (Fig. 2D). Similar drug release behaviors were observed for PAF NPs. This ultrasound-promoted drug release from the NP samples is likely attributable to ROS generation upon ultrasonication of ART (to be discussed below). The resultant ROS would oxidize the thioether units in the PPMDT core of the nanoparticles, causing the particles to swell to accelerate the drug release. As shown in Figs. S5–C, the ROS caused by ultrasonic and acidic environment could achieve synergistic promotion on further ROS response of PEG-PPMDT NPs and faster drug release of ART.

3.5. ROS generation by ultrasonication or acidification of ART-loaded NPs

The ultrasound-promoted ROS generation by ART in PEG-PPMDT NPs was investigated in PBS solutions containing DPBF at various pH values. Upon continuous ultrasonication (1 MHz, 2 W/cm²) in PBS (pH 7.4), both PA NPs and PAF NPs were found to rapidly generate ROS which subsequently reacted with DPBF, and the DPBF absorption at 413 nm was substantially reduced within 10 min (Fig. 2E). For comparison, unlike free ART, neither the blank PEG-PPMDT micelles nor Fe₃O₄ NPs are capable of producing ROS under same conditions. Presumably, the ROS intermediates were produced via facile cleavage of the bridging peroxide bond in ART by highly energetic ultrasound irradiation. Consistently, the rate of ROS generation in PBS with pH 7.4 was essentially identical for the PA NPs and PAF NPs containing the same amount of ART load (Fig. 2E). It is notable that without ultrasound irradiation, the rate of ROS generation by PAF NPs in PBS is highly pH-dependent with lower pH increasing the rate (Fig. 2F). This is expected since free Fe²⁺ ions released from Fe₃O₄ NPs under acidic conditions would react with ART to produce ROS, which can gradually reduce the concentration of co-dissolved DPBF. These results demonstrate that PAF NPs are capable of self-generating exogenous ROS in acidic tumor tissue or in acidic endosomes/lysosomes of tumor cells. The exogenous ROS production in tumor can be further amplified by external ultrasound irradiation for fast killing of tumor cells, which constitutes an important part of current chemo-sonodynamic antitumor therapy.

3.6. Cytotoxicity

The cytotoxicity of free ART was investigated using HepG2 cells. The cell viability is dose-dependent and decreases with increasing ART

concentration (Figs. S6–A). As shown in Fig. 3A, both external ultrasound irradiation (1 MHz, 2 W/cm², 3 min) and free Fe²⁺ ions (FeCl₂, 0.05 mM) enhance the ART cytotoxicity. Fe²⁺ ions released from Fe₃O₄ NPs under mildly acidic conditions (pH 6.5) are equally effective in promoting the cytotoxicity of ART. Notably, free Fe³⁺ (FeCl₃, 0.05 mM) or Fe²⁺ ions (FeCl₂, 0.05 mM) alone and blank PEG-PPMDT NPs are nontoxic toward HepG2 cells, and neither Fe³⁺ ions nor stable Fe₃O₄ NPs at physiological pH of 7.4 affect the ART cytotoxicity (Fig. 3A and Figs. S6–B, C). These results are in accord with the previous data suggesting that ultrasonication or acidification of PAF NPs triggers rapid *in vitro* ROS production (Fig. 2E and F). Thus, the enhancement of ART cytotoxicity by ultrasound irradiation and free Fe²⁺ ions is likely due to ROS production in the processes, accelerating the killing of HepG2 cells.

To assess synergistic anticancer effects of stimulus response and combined chemo-sonodynamic therapy, the cytotoxicity values of ART-loaded PEG-PPMDT (PA) NPs and ART/Fe₃O₄-loaded PEG-PPMDT (PAF) NPs against HepG2 cells were measured under different pH conditions with or without ultrasound irradiation. As demonstrated in Fig. 3B and C, the ART-loaded PEG-PPMDT NPs showed dose-dependent cytotoxicity with higher drug concentration reducing cell viability. For PA NPs, the viability of HepG2 cells was lower upon ultrasonication, but was minimally affected by pH (Fig. 3B). In contrast, the cytotoxicity of PAF NPs increased both upon ultrasonication and by lowering the medium pH from 7.4 to 6.5 (Fig. 3C). As discussed above, ultrasound irradiation, as well as free Fe²⁺ ions released from Fe₃O₄ NPs in acidic medium, can effectively promote ART decomposition to form ROS for accelerated killing of the cancer cells. The synergistic effects of ultrasonication and acidification on the cytotoxicity of PAF NPs are important, signifying that PAF NPs are capable of exerting enhanced toxicity towards tumor cells in acidic tumor tissue or the cell endosomes and upon external ultrasonication at the tumor site.

3.7. Cellular uptake

Coumarin 6 (C6) was encapsulated in PEG-PPMDT NPs to study their cellular uptake and intracellular distribution. The uptake of C6-loaded PEG-PPMDT NPs and free C6 by HepG2 cells was analyzed by flow cytometry, and the results are shown in Fig. 3D–F. The fluorescence intensity of both samples gradually increased from 1 to 6 h, then decreased from 6 to 8 h during the 8-h incubation (Fig. 3D and E). Notably, the MFI values were consistently higher for the C6-loaded micelles vs free C6, which is likely attributable to different cellular uptake pathways for the two samples (Fig. 3F).

The intracellular distribution of C6-loaded PEG-PPMDT NPs and free C6 in the HepG2 cells were observed by CLSM (Fig. 3G). Consistent with the above flow cytometry results, the C6-loaded micelles were evenly distributed throughout the cytoplasm after 6-h incubation. Free C6 could be rapidly enriched in tumor cells by free diffusion and quickly excluded from cells at 12 h. In C6-loaded PEG-PPMDT NPs group, it was found that the fluorescence of C6 and lysosomes displayed comparative colocalization within 1h, indicating that NPs entered tumor cells by endocytosis. After 6 h of incubation, C6-loaded PEG-PPMDT NPs were evenly distributed throughout the cytoplasm and showed good lysosomal escape ability, which could increase the cytotoxicity of the drug-loaded PEG-PPMDT NPs.

3.8. Intracellular ROS production

The intracellular ROS generation by ART in PEG-PPMDT NPs was investigated by flow cytometry and CLSM using 2',7'-dichlorodihydrofluorescein diacetate (DCF-DA) as a ROS-detecting agent. As shown in Fig. 4A–C, the change of pH from 7.4 to 6.5 only slightly affected the ability of PA NPs to produce intracellular ROS. In contrast, the ROS level yielded by PAF NPs was substantially higher at pH 6.5 vs pH 7.4 since free Fe²⁺ ions released by the Fe₃O₄ NPs in acidic medium can reduce ART to generate ROS. ART is an effective sonosensitizer capable of

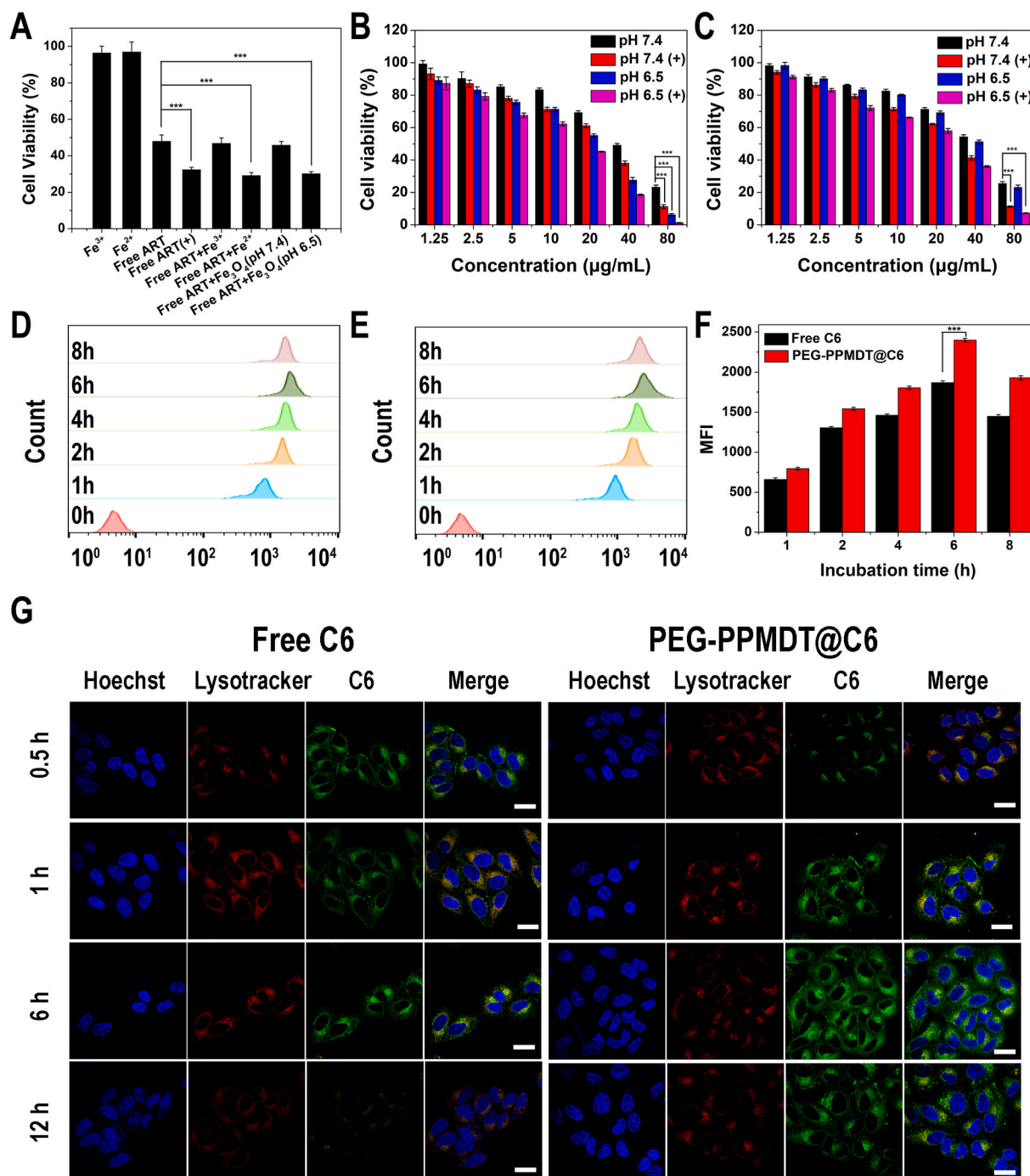


Fig. 3. (A) The viabilities of HepG2 cells incubated with different pH culture media containing one or more components: Fe²⁺, Fe³⁺, Fe₃O₄ NPs and ART (40 µg/mL). (+) represents additional ultrasound irradiation treatment (1 MHz, 2 W/cm², 3 min). The viabilities of HepG2 cells treated with (B) PA NPs and (C) PAF NPs in acidic or neutral PBS with/without ultrasound irradiation (mean ± SD, n = 5). Fluorescence histograms of HepG2 cells treated with free C6 (D) and C6-loaded PEG-PPMDT micelles (E), and the corresponding intracellular C6 MFI values after 1–8 h incubation (F). CLSM images of the intracellular free C6 and C6-loaded micelles (G) after 6-h incubation with HepG2 cells. Scale bar = 20 µm *p < 0.05, **p < 0.01 and ***p < 0.001.

producing ROS upon ultrasonication. Thus, ultrasound irradiation remarkably enhances the intracellular ROS generation by both PA NPs and PAF NPs (Fig. 4C). Importantly, with the synergistic effects of acidification and ultrasonication, PAF NPs exhibit the highest ROS-generation capability at tumor-relevant, acidic pH under ultrasound irradiation. These flow cytometry results were confirmed by the CLSM images induced by the ROS intermediates (Fig. 4D and E). As we demonstrate in latter sections, such amplified intracellular ROS generation not only can directly cause apoptosis of tumor cells, but also can

further accelerate the drug release from ROS-responsive PEG-PPMDT NPs, yielding excellent efficacy of our chemo-sonodynamic therapy based on PAF NPs.

3.9. Cellular apoptosis

HepG2 cells were incubated with PA and PAF NPs under different pH and ultrasonication conditions, and the cell apoptosis levels were evaluated by flow cytometry. As exhibited in Fig. 5A, C, the apoptosis value

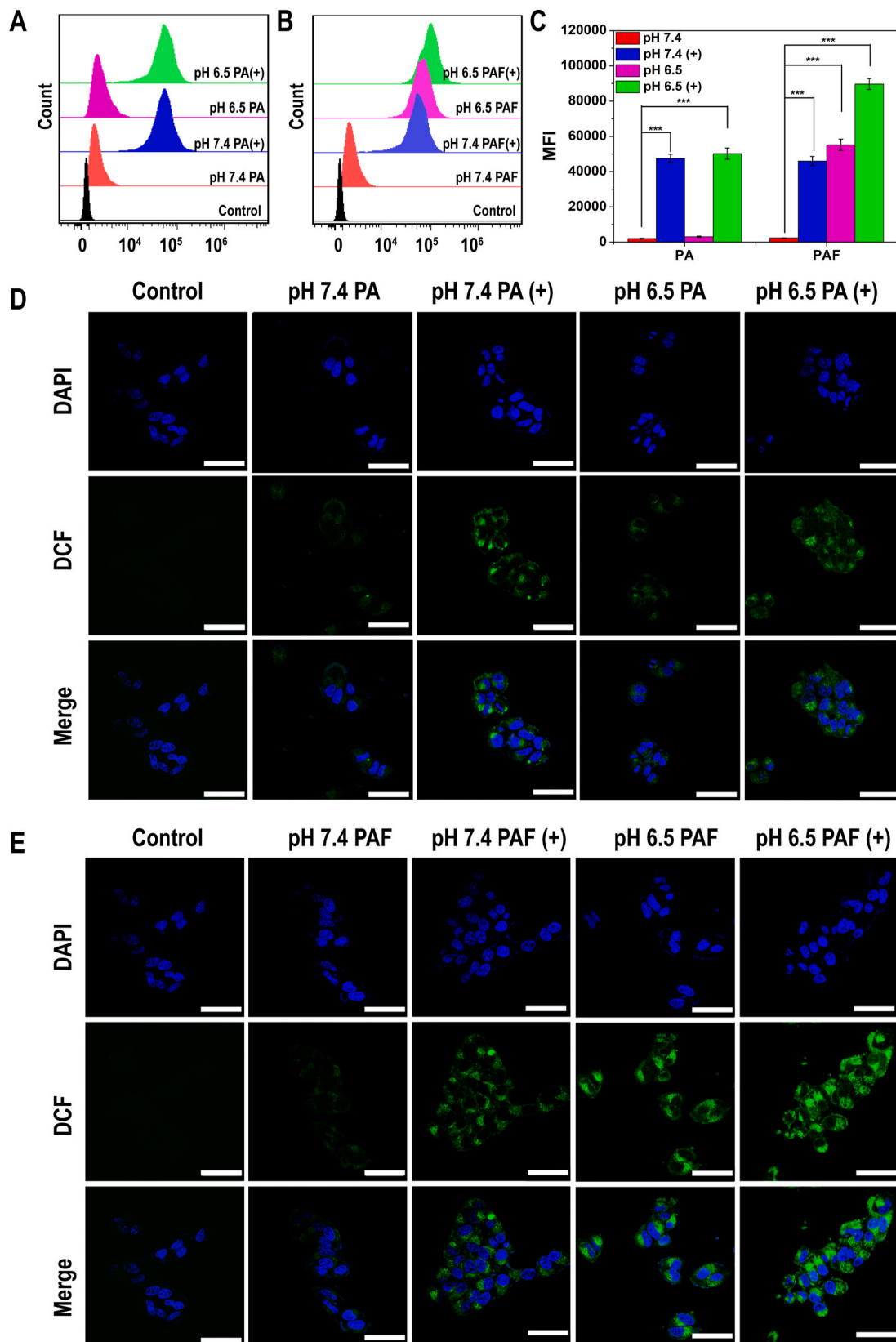


Fig. 4. Fluorescence histograms of the ROS produced by ART-loaded PEG-PPMDT NPs (A) and ART/Fe₃O₄-loaded PEG-PPMDT NPs (B) in HepG2 cells with or without ultrasonication in media with different pH, the corresponding mean fluorescence intensity values (C), and CLSM images of ART-loaded PEG-PPMDT NPs (D) and ART/Fe₃O₄-loaded PEG-PPMDT NPs (E) due to the ROS intermediates. (+) represents additional ultrasound irradiation (1 MHz, 2 W/cm², 3 min). Scale bar = 50 μm **p* < 0.05, ***p* < 0.01 and ****p* < 0.001.

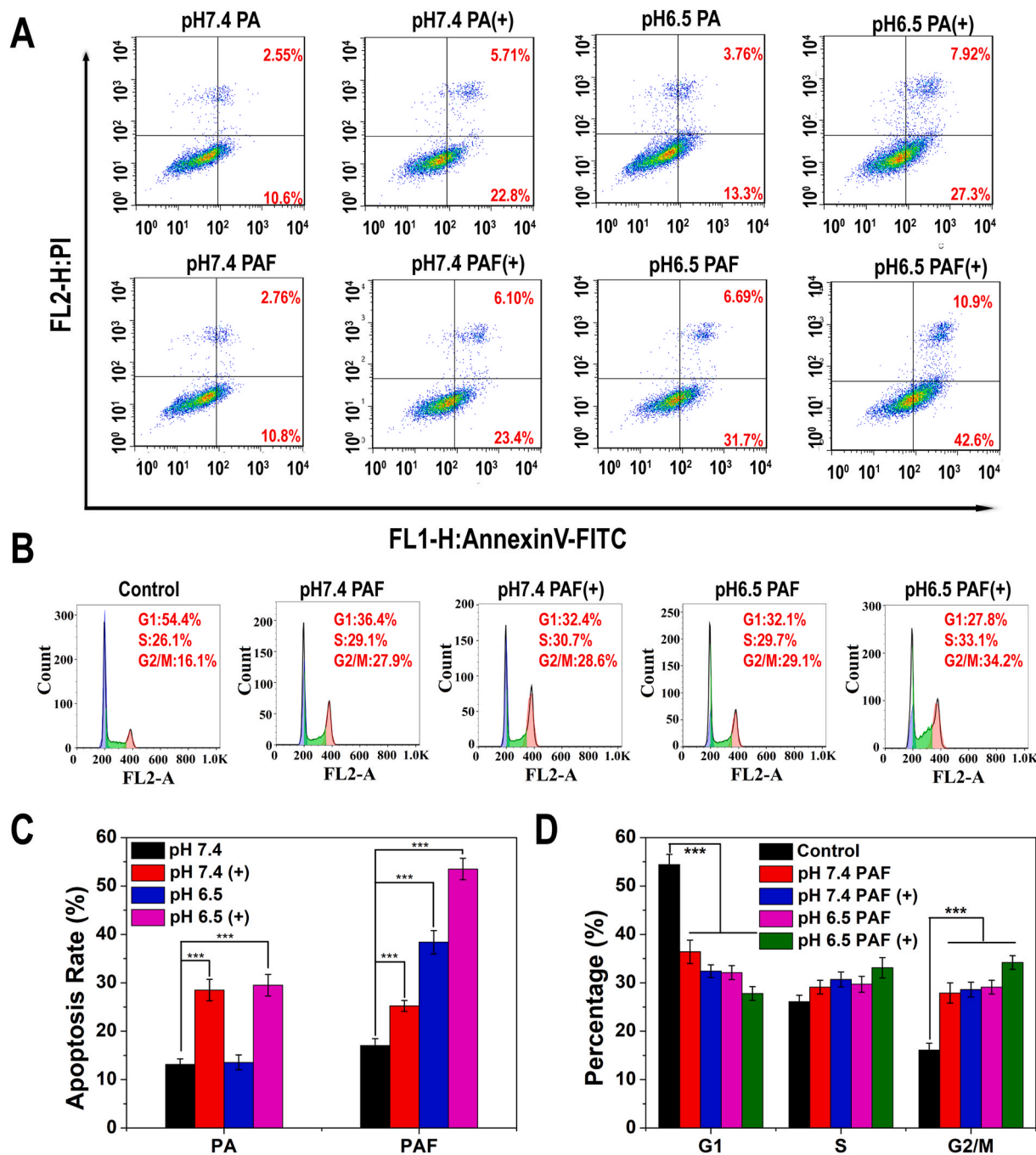


Fig. 5. Apoptosis results (A, C) and cell cycle analysis (B, D) of HepG2 cells incubated with ART-loaded or ART/Fe₃O₄-loaded PEG-PPMDT micelles with or without ultrasonication in the media of different pH (mean ± SD, n = 5). (+) represents additional ultrasound irradiation (1 MHz, 2 W/cm², 3 min). **p* < 0.05, ***p* < 0.01 and ****p* < 0.001.

for PA NPs-treated cell group increased slightly upon varying pH from 7.4 to 6.5 (13% vs 17%), and more significantly upon ultrasonication (29% vs 13% at pH 7.4, 35% vs 17% at pH 6.5). In contrast, acidification had substantially more effects on apoptosis of the cells treated by PAF NPs (14% at pH 7.4 vs 38% at pH 6.5), whereas ultrasonication similarly enhanced the apoptosis (30% vs 14% at pH 7.4, 54% vs 38% at pH 6.5). Consistent with the earlier results, these data confirm that ultrasonication and free Fe²⁺ ions formed from Fe₃O₄ of PAF NPs in acidic medium can efficiently activate ART to produce ROS, thus synergistically promoting cell apoptosis. Among the various treated cell groups, the best cell apoptosis rate (~54%) was observed for the PAF NPs group ultrasonicated at tumor-relevant pH of 6.5 (Fig. 5A). This is another

important reason why we subsequently chose to focus on PAF NPs for *in vivo* chemo-sonodynamic antitumor experiments (to be discussed in a latter section).

3.10. Cell cycle

The cell cycle phase distribution of HepG2 cells treated by PAF NPs under different ultrasonication (US) and pH conditions was determined by flow cytometry. In Fig. 5B, D, the control cell group had 54.4% cell population in G1 phase and 16.1% population in G2/M phase. In contrast, the cell groups of pH 7.4 PAF, pH 7.4 PAF (+), pH 6.5 PAF and pH 6.5 PAF (+) possessed lower G1 phase populations of 36.4%, 32.4%,

32.1%, 27.8%, but higher G2/M phase populations of 27.9%, 28.6%, 29.1%, 34.2%, respectively. Clearly, upon incubation with ART, the cell population of G1 phase decreased whereas those of G2/M phase increased, indicating that ART primarily affected the prophase and mitotic phase of cell cycle regardless of ultrasound irradiation. These

results are consistent with previous literature reports showing that artemether can block the cell cycle in G2/M phase [57]. Since the ROS produced by artemether also inhibit cell proliferation, the G1 phase cell population were reduced synergistically by ultrasonication and acidification.

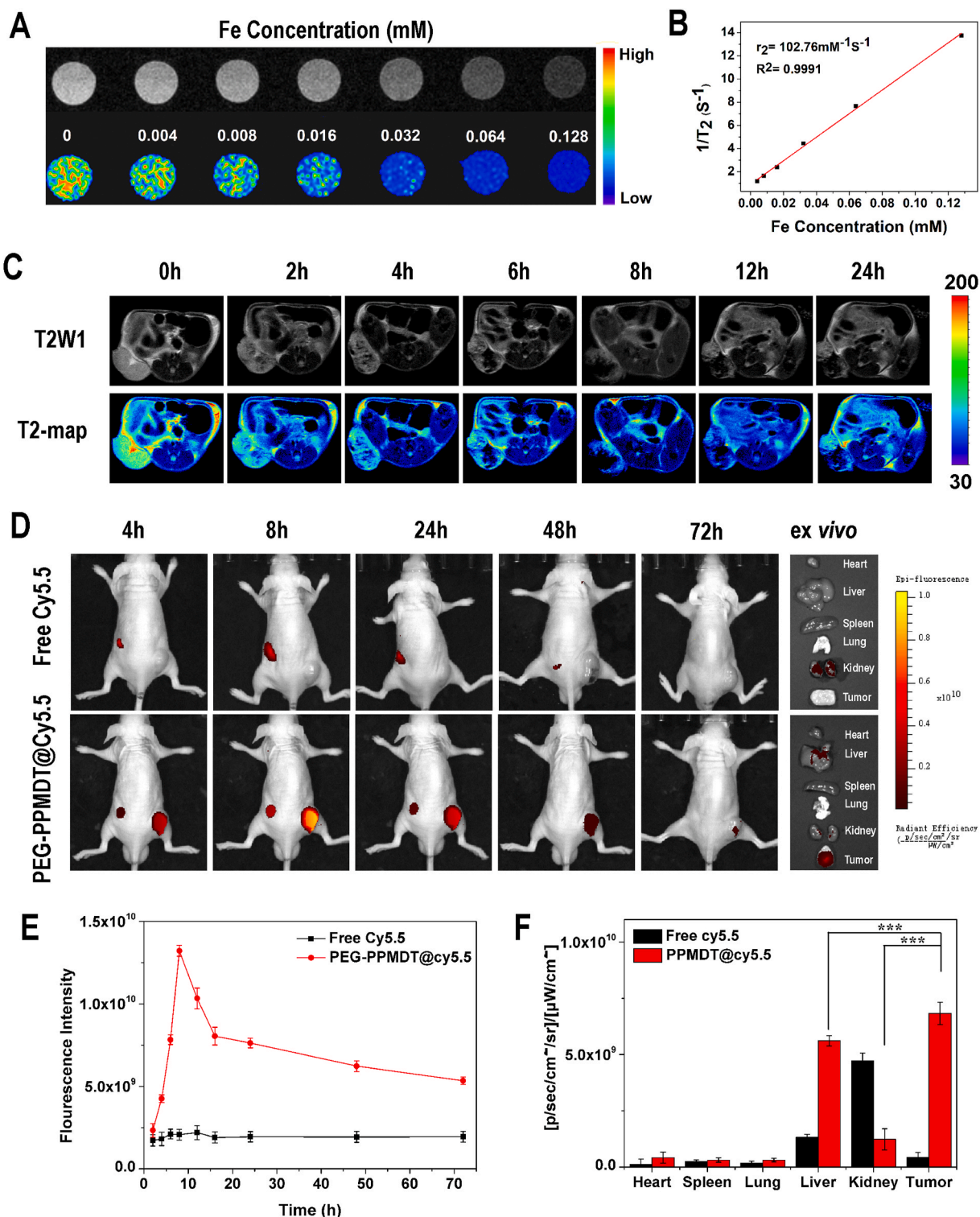


Fig. 6. T₂-weighted MRI images (A) and the linear correlation between T₂ relaxation rate R₂ (1/T₂) and iron concentration (B) of PAF NPs suspended in pH 7.4 PBS, (C) *in vivo* T₂-weighted MR imaging and T₂-map of the PAF NPs, (D) *in vivo* fluorescence imaging of Cy5.5-loaded PEG-PPMDT micelles and free Cy5.5 in HepG2 tumor-bearing mice and *ex vivo* fluorescence images of major organs and tumors at 72 h post-injection, (E) quantification of average fluorescence intensities at the tumor site, (F) quantification of the fluorescent signals associated with the major organs and tumors. Data is given as mean ± SD (n = 3). *p < 0.05, **p < 0.01 and ***p < 0.001.

3.11. MRI imaging in vitro and in vivo

To evaluate the MRI potential of PAF NPs *in vivo*, we performed T₂ weighted MR imaging to measure the T₂-weighted relaxivity (r₂). With the increase of iron concentration, T₂-weighted MR imaging signal became stronger, resulting in a darker image (Fig. 6A). In order to demonstrate the dose-dependent enhancement of MRI contrast clearly, we quantitatively analyzed the linear correlation between the R₂ (1/T₂) values of ART/Fe₃O₄-loaded PEG-PPMDT NPs and iron concentration (Fig. 6B). The high r₂ value (102.76 s⁻¹ mM⁻¹) of PAF NPs indicates that the NPs are adequate to serve as an effective MRI T₂ contrast agent to observe the drug delivery *in vivo*.

The *in vivo* MRI imaging experiments based on PAF NPs were investigated using a mouse model bearing HepG2 tumor. After PAF NPs were injected intravenously into the tumor-bearing mice, the signal intensity of T₂ scan at the tumor site gradually increased and the brightness gradually decreased from 0 to 8 h (Fig. 6C). Consistently, as shown in Fig. S7, the T₂ signal intensity in tumor area decreased continuously from 0 to 8 h post injection, reached the lowest value (corresponding to

the highest contrast enhancement ratio of 170%) at 8 h vs the control group, and then recovered slowly from 8 to 24 h due to the clearance of iron. The results confirm that PAF NPs can effectively aggregate to tumor site *in vivo* through EPR effect, and act as a promising MRI T₂ probe for solid tumors to guide procedures of current chemosonodynamic therapy.

3.12. Biodistribution

Cy5.5-loaded PEG-PPMDT NPs were employed to evaluate the NPs biodistribution *in vivo*, which was monitored by a real-time NIR fluorescence imaging technique at various time intervals. As shown in Fig. 6D, free Cy5.5 was mainly distributed in kidney with negligible accumulation in the tumor, and the fluorescence intensity of the tumor site hardly changed within 72 h. In contrast, Cy5.5-loaded PEG-PPMDT NPs rapidly aggregated to the tumor site within 4 h after injection, eliciting the maximum fluorescence intensity at 8 h. And the fluorescence images of the major organs (including tumors) harvested from the mice at 72 h shows that free Cy5.5 primarily accumulated in the kidney

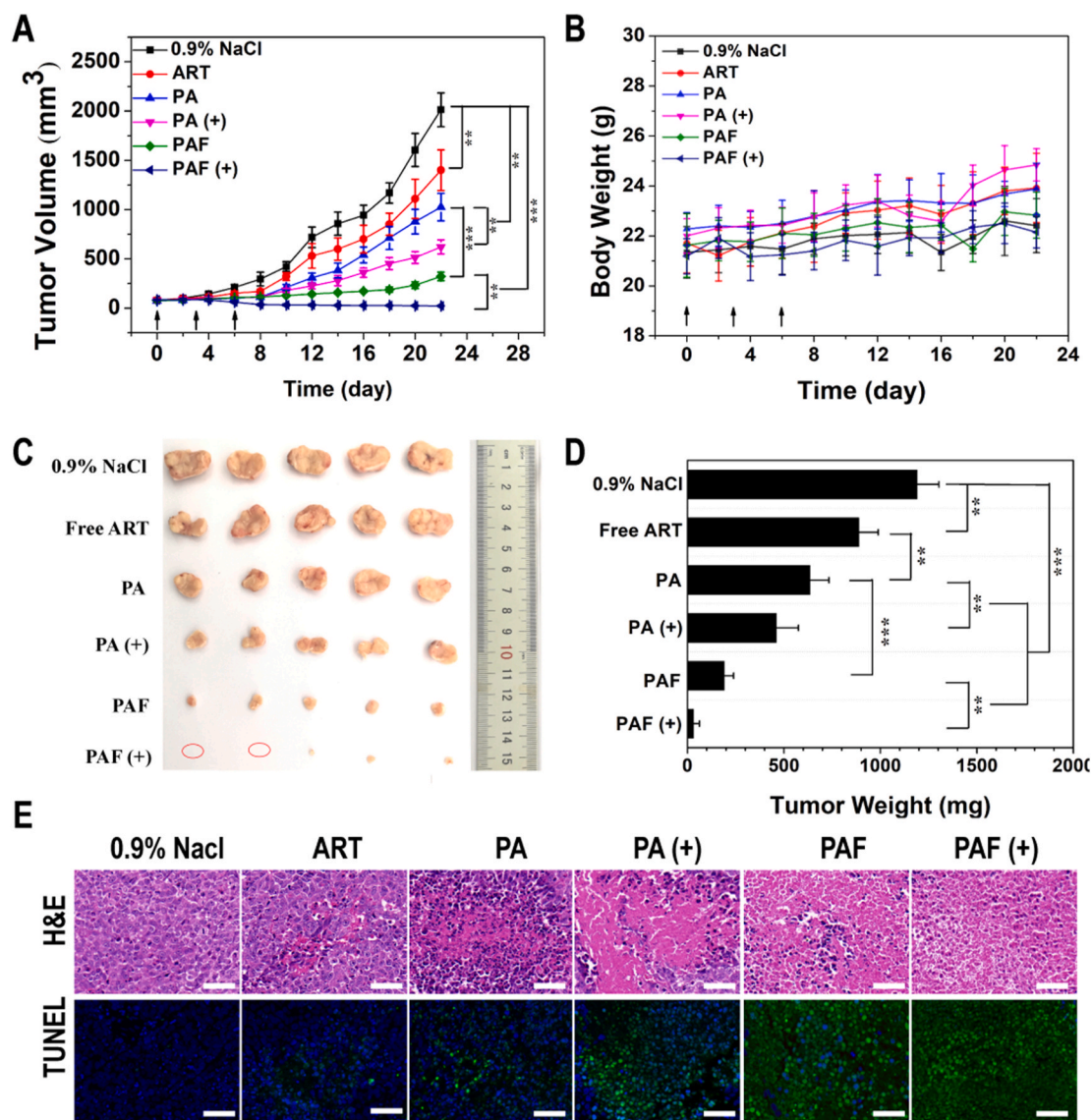


Fig. 7. Variations in tumor volume (A) and body weight (B) of the mice treated with 0.9% NaCl, free ART, ART-loaded PEG-PPMDT NPs and ART/Fe₃O₄-loaded PEG-PPMDT NPs with or without ultrasound treatment (1 MHz, 2 W/cm², 10 min), the morphology (C) and weight (D) of the harvested tumors on 22nd day, (E) the images of tumor tissue sections stained by H&E and TUNEL. (+) represents additional ultrasound irradiation treatment (1 MHz, 2 W/cm², 10 min). Scale bar = 50 μm. Data are given as mean ± S.D. (n = 5). *p < 0.05, **p < 0.01 and ***p < 0.001.

and was excreted with minimal aggregation in tumor. The subsequent gradual decrease of the fluorescence intensity implies that the NPs had a prolonged circulation time to passively target the tumor (Fig. 6E). In stark contrast, the mice treated with Cy5.5-loaded PEG-PPMDT NPs exhibited highest fluorescence intensity in the tumor due to the passive targeting mechanism of EPR effect (Fig. 6F). Together, these data demonstrate that the PEG-PPMDT NPs possess a prolonged blood circulation time, and can preferentially deliver drug to tumor areas, thus minimizing the systemic toxicity of chemotherapy drugs.

3.13. Antitumor efficacy *in vivo*

HepG2 tumor-bearing nude mice were employed to access the *in vivo* antitumor efficiency of ART/Fe₃O₄-loaded PEG-PPMDT (PAF) NPs. Briefly, the mice with approximately 100 mm³ tumors were randomly divided into six groups: (i) 0.9% NaCl, (ii) free ART, (iii) PA NPs, (iv) PA NPs (+), (v) PAF NPs, (vi) PAF NPs (+). The sign (+) represents additional ultrasound irradiation (1 MHz, 2 W/cm², 10 min). As shown in Fig. 7A, rapid tumor growth was observed in the control group during the 22-day antitumor treatment. In comparison, free ART and PA NPs moderately inhibited the tumor growth. The antitumor efficacy was further enhanced when the mice were treated by PAF NPs and by PA NPs with ultrasonication (US). In both cases, ROS production in tumor is amplified by interactions of ART with free Fe²⁺ ions (formed from Fe₃O₄ of PAF NPs in acidic tumor matrix or endosomes) or with ultrasound irradiation, which can not only directly elicit cytotoxicity to tumor cells, but also along with acidic pH and elevated intracellular GSH, accelerate the release of ART from the pH, GSH, ROS triple-responsive PEG-PPMDT NPs to boost chemotherapeutic efficacy. The best treatment result was obtained for the PAF NPs group with ultrasonication due to synergistic ROS generation by ART/Fe²⁺ and ART/ultrasound interactions. As a result, all tumors in the PAF NPs (+) group shrank substantially with 40% tumors (in two out of five mice) being completely eradicated. Specifically, at the end of antitumor therapy (day 22), the mean tumor volumes of 0.9% NaCl, free ART, PA NPs, PA NPs (+), PAF NPs, PAF NPs (+) groups were 2013, 1400, 1025, 621, 321, 22 mm³, respectively. The tumors harvested from the mice at day 22 were photographed and weighed (Fig. 7C and D), and the results are accordant with the tumor growth data in Fig. 7A. The extraordinary antitumor efficacy of the chemo-sonodynamic therapy based on PAF NPs shows powerful effects of a combined, multi-functional therapeutic method and is attributable to the following factors: (i) prolonged blood circulation time of PAF NPs to allow their preferential aggregation to tumor through the EPR effect, (ii) accelerated drug release triggered by acidic endosomal pH and intracellular high GSH/ROS concentrations after absorption of the NPs by the tumor cells, and (iii) synergistically amplified ROS generation in tumor by ART via interactions with Fe²⁺ ions formed *in situ* and with external ultrasound irradiation. Further, during the therapeutic procedures, there were no significant changes in mouse body weight for all groups, indicating good potential of therapeutic safety for the PEG-PPMDT NP formulations (Fig. 7B). Besides the mice in PA, PAF and PAF (+) groups survived for over 22 days without a death until they were executed, while all the mice of other groups died or exceeded the established end-value 1000 mm³ in 16–22 days after treatment (Fig. S8), indicating the ROS level of NPs-treated tumor cells magnified by ART *in situ* or external ultrasound irradiation could effectively prolong the survival time of the mice.

H&E and TUNEL staining of the harvested tumor tissues is shown in Fig. 7E. As depicted in the H&E staining images (Fig. 7E, up panel), the tumor tissue of the control group (0.9% NaCl) displayed malignant hyperplasia and was closely arranged. In contrast, a few tumor cells in free ART group were atrophied due to nuclear pyknosis and chromatin condensation. Significantly, distinct cell shrink and necrosis were observed in all nanoparticle groups. The sample of PAF NPs (+) group exhibited most apoptotic tumor cells with pyknosis and broken cell membrane, confirming the outstanding *in vivo* antitumor efficacy of the

combined chemo-sonodynamic therapy. Tumor apoptosis after the 22-day treatments was also analyzed by TUNEL staining to further validate the antitumor effects. Apoptotic cells were stained green with normal nuclei stained blue. Consistent with the results of H&E staining, there was no obvious apoptotic marker in the 0.9% NaCl group, and PAF NPs (+) group showed most abundant TUNEL-positive cells (Fig. 7E, low panel).

3.14. Biosafety

H&E staining of normal organ sections and serum biochemical analysis were performed to estimate the biosafety of PA NPs and PAF NPs for clinical applications. The heart, liver, spleen, lung and kidney were excised from the tumor-bearing mice and analyzed by H&E staining. The results show that all treatments, including those with PA NPs, PA NPs (+), PAF NPs and PAF NPs (+), did not induce obvious toxicity to these main organs (Fig. 8A). Further, biochemical analyses were performed to determine the myocardial toxicity (level of CK), nephrotoxicity (levels of BUN, CRE) and hepatotoxicity (levels of ALT, AST, ALP) of the NPs. The indexes of liver, renal and myocardial function in each treatment group were not significantly increased or decreased compared to 0.9% NaCl control group (Fig. 8B). It's also notable that blank PEG-PPMDT NPs are hemocompatible and possess minimal hemolytic activity (<2% hemolysis) at 500 µg/mL (Fig. S9). These results confirm that ART/Fe₃O₄-loaded PEG-PPMDT NPs have good safety potential for stimuli-responsive, combined chemo-sonodynamic antitumor therapy.

4. Conclusion

We have designed and developed a potent, ROS-amplifying chemo-sonodynamic antitumor therapy based on novel pH/GSH/ROS triple-responsive PEG-PPMDT nanoparticles. The formulated ART/Fe₃O₄-loaded PEG-PPMDT NPs show excellent stability in aqueous medium containing serum and can effectively aggregate into tumor site via passive targeting mechanism due to the EPR effect *in vivo*. Upon internalization by tumor cells, and in response to high intracellular GSH/ROS concentrations and acidic endosomal environment, the PEG-PPMDT NPs can rapidly unload the therapeutic drug to kill the cells. In the designed chemo-sonodynamic therapy, the intracellular ROS production is amplified by ART via interactions with both Fe²⁺ ions formed *in situ* at acidic pH and external ultrasound irradiation, hence eliminating therapeutic resistance due to hypoxic tumor microenvironments. As a result, the excessively high concentration of intracellular ROS can directly kill tumor cells and further accelerate the drug release from the ROS-responsive PEG-PPMDT NPs to achieve outstanding antitumor efficacy. Specifically, upon the chemo-sonodynamic therapy by ART/Fe₃O₄-loaded PEG-PPMDT NPs, all xenotransplants of human hepatocellular carcinoma (HepG2) in nude mice shrank substantially with 40% of the tumors being completely eliminated. Importantly, the Fe₃O₄ encapsulated in the NPs is an efficient MRI contrast agent and can be used to guide the therapeutic procedures. Further, biosafety analyses show that the PEG-PPMDT NPs possess minimal toxicity to normal organs. Thus, our combined chemo-sonodynamic therapeutic method is promising for potent antitumor treatment by controlled release of drug and facile exogenous generation of abundant ROS at target tumor sites.

Data availability

The raw/processed data required to reproduce these findings cannot be shared at this time due to technical or time limitations.

CRediT authorship contribution statement

JunJie Tang: Conceptualization, Methodology, Formal analysis, Data curation, Writing – original draft, Writing – review & editing.

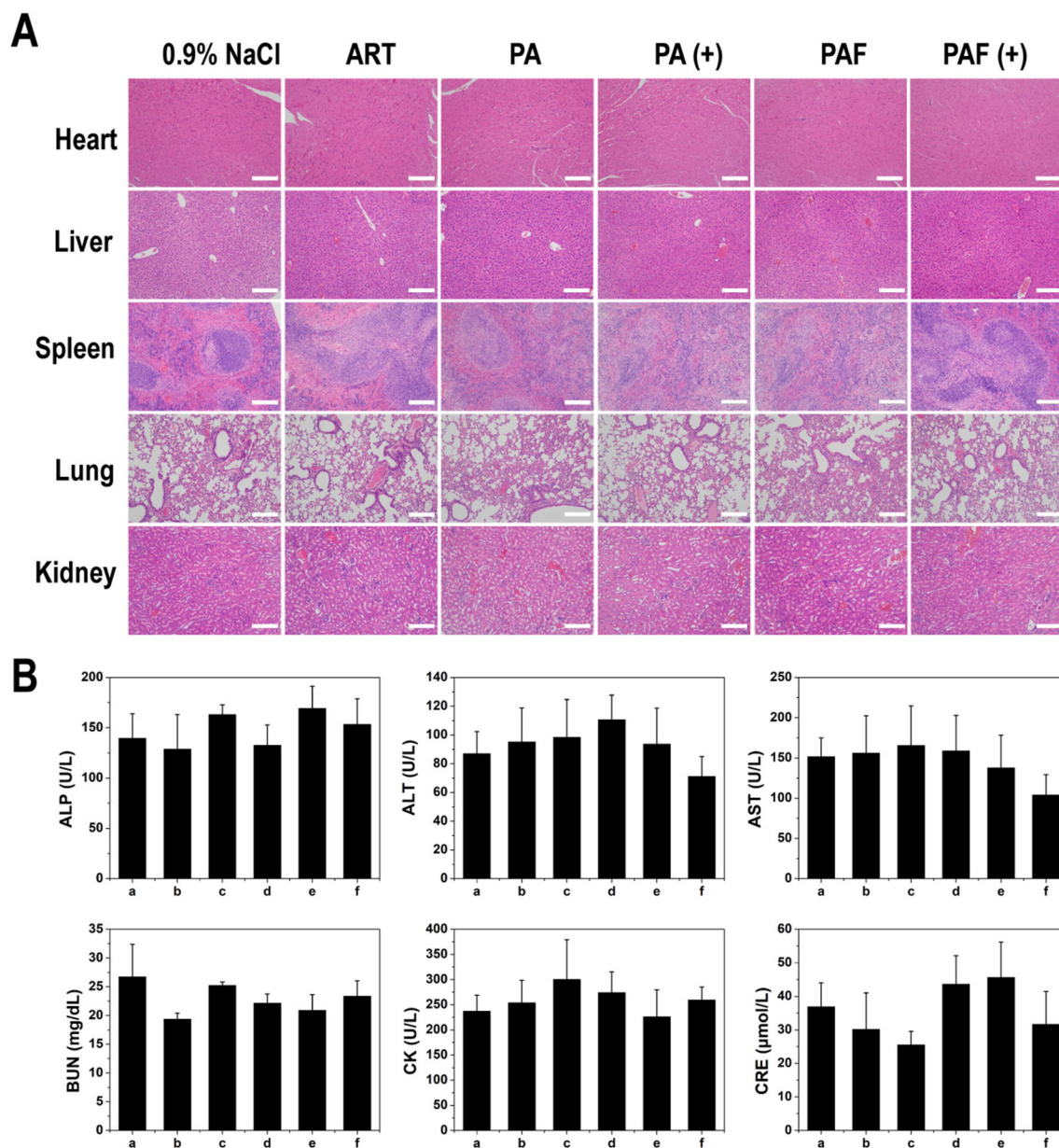


Fig. 8. (A) H&E staining results of normal organs (heart, liver, spleen, lung, and kidney) from mice in the treatment groups on the 22nd day, and (B) serum biochemical analysis of the mice treated with 0.9% NaCl (a), free ART (b), PA NPs and PAF NPs without ultrasonication (c, d) or with ultrasonication (e, f). (+) represents additional ultrasound irradiation treatment (1 MHz, 2 W/cm², 10 min). Scale bar = 100 μm.

Xiaoge Zhang: Investigation, Formal analysis, Writing – review & editing. **Lili Cheng:** Investigation, Methodology. **Yadong Liu:** Investigation, Validation. **You Chen:** Investigation, Validation. **Zhaozhong Jiang:** Conceptualization, Writing – original draft, Writing – review & editing, Project administration, Funding acquisition. **Jie Liu:** Conceptualization, Writing – original draft, Writing – review & editing, Supervision, Project administration, Funding acquisition.

Declaration of competing interest

The authors declare that they have no known competing financial interests or personal relationships that could have appeared to influence the work reported in this paper.

Acknowledgements

This work was supported by the National Natural Science Foundation

of China (51773231), the Natural Science Foundation of Guangdong Province (2016A030313315), Shenzhen Science and Technology Project (JCYJ20190807160801664), the Project of Key Laboratory of Sensing Technology and Biomedical Instruments of Guangdong Province (2011A060901013). We also appreciate Yale University for providing private funds to support synthesis of the biomaterials.

Appendix A. Supplementary data

Supplementary data to this article can be found online at <https://doi.org/10.1016/j.bioactmat.2021.12.002>.

References

[1] L.-Q. Zhou, P. Li, X.-W. Cui, C.F. Dietrich, Ultrasound nanotheranostics in fighting cancer: advances and prospects, *Cancer Lett* 470 (2020) 204–219.

- [2] S. Son, J.H. Kim, X. Wang, C. Zhang, S.A. Yoon, J. Shin, A. Sharma, M.H. Lee, L. Cheng, J. Wu, J.S. Kim, Multifunctional sonosensitizers in sonodynamic cancer therapy, *Chem. Soc. Rev.* 49 (2020) 3244–3261.
- [3] X.Q. Qian, Y.Y. Zheng, Y. Chen, Micro/nanoparticle-augmented sonodynamic therapy (SDT): breaking the depth shallow of photoactivation, *Adv. Mater.* 28 (2016) 8097–8129.
- [4] X. Pan, H. Wang, S. Wang, X. Sun, L. Wang, W. Wang, H. Shen, H. Liu, Sonodynamic therapy (SDT): a novel strategy for cancer nanotheranostics, *Sci. China: Life Sci.* 61 (2018) 415–426.
- [5] X.W. Cui, X.X. Han, L.D. Yu, B. Zhang, Y. Chen, Intrinsic chemistry and design principle of ultrasound-responsive nanomedicine, *Nano Today* 28 (2019).
- [6] H.J. Chen, X.B. Zhou, Y. Gao, B.Y. Zheng, F.X. Tang, J.D. Huang, Recent progress in development of new sonosensitizers for sonodynamic cancer therapy, *Drug Discovery Today* 19 (2014) 502–509.
- [7] A. Ma, H. Chen, Y. Cui, Z. Luo, R. Liang, Z. Wu, Z. Chen, T. Yin, J. Ni, M. Zheng, L. Cai, Metalloporphyrin complex-based nanosensitizers for deep-tissue tumor theranostics by noninvasive sonodynamic therapy, *Small* 15 (2019).
- [8] X. Lin, S. Liu, X. Zhang, R. Zhu, S. Chen, X. Chen, J. Song, H. Yang, An ultrasound activated vesicle of janus Au-MnO₂ nanoparticles for promoted tumor penetration and sono-chemodynamic therapy of orthotopic liver cancer, *Angew. Chem., Int. Ed.* 59 (2020) 1682–1688.
- [9] M. Liu, A.R. Khan, J. Ji, G. Lin, X. Zhao, G. Zhai, Crosslinked self-assembled nanoparticles for chemo-sonodynamic combination therapy favoring antitumor, antimetastasis management and immune responses, *J. Controlled Release* 290 (2018) 150–164.
- [10] H. Xu, M. Hu, M. Liu, S. An, K. Guan, M. Wang, L. Li, J. Zhang, J. Li, L. Huang, Nano-puerarin regulates tumor microenvironment and facilitates chemo- and immunotherapy in murine triple negative breast cancer model, *Biomaterials* (2020) 235.
- [11] M. Liu, W. Song, L. Huang, Drug delivery systems targeting tumor-associated fibroblasts for cancer immunotherapy, *Cancer Lett* 448 (2019) 31–39.
- [12] J. An, Y.-G. Hu, C. Li, X.-L. Hou, K. Cheng, B. Zhang, R.-Y. Zhang, D.-Y. Li, S.-J. Liu, B. Liu, D. Zhu, Y.-D. Zhao, A pH/Ultrasound dual-response biomimetic nanopatform for nitric oxide gas-sonodynamic combined therapy and repeated ultrasound for relieving hypoxia, *Biomaterials* (2020) 230.
- [13] S. Liang, X. Deng, Y. Chang, C. Sun, S. Shao, Z. Xie, X. Xiao, P.a. Ma, H. Zhang, Z. Cheng, J. Lin, Intelligent hollow Pt-CuS janus architecture for synergistic catalysis-enhanced sonodynamic and photothermal cancer therapy, *Nano Lett* 19 (2019) 4134–4145.
- [14] J. Chen, H.L. Luo, Y. Liu, W. Zhang, H.X. Li, T. Luo, K. Zhang, Y.X. Zhao, J.J. Liu, Oxygen-self-produced nanopatform for relieving hypoxia and breaking resistance to sonodynamic treatment of pancreatic cancer, *ACS Nano* 11 (2017) 12849–12862.
- [15] H. Mei, X. Zhang, S. Cai, X. Zhang, Y. Zhang, Z. Guo, W. Shi, R. Chu, K. Zhang, J. Cao, B. He, Fluorocarbon-driven photosensitizer assembly decodes energy conversion pathway for suppressing breast tumor, *Nano Today* 41 (2021).
- [16] T. Luo, D. Wang, L. Liu, Y. Zhang, C. Han, Y. Xie, Y. Liu, J. Liang, G. Qiu, H. Li, D. Su, J. Liu, K. Zhang, Switching reactive oxygen species into reactive nitrogen species by photocleaved O₂-Released nanopatforms favors hypoxic tumor repression, *Adv. Sci.* 8 (2021).
- [17] H. Nosrati, R. Aramideh Khoyi, A. Nosrati, M. Khodaei, M. Banitalebi-Dehkordi, K. Ashrafi-Dehkordi, S. Sanami, Z. Alizadeh, Nanocomposite scaffolds for accelerating chronic wound healing by enhancing angiogenesis, *J. Nanobiotechnol.* 19 (2021).
- [18] X. Guan, H.-H. Yin, X.-H. Xu, G. Xu, Y. Zhang, B.-G. Zhou, W.-W. Yue, C. Liu, L.-P. Sun, H.-X. Xu, K. Zhang, Tumor metabolism-engineered composite nanopatforms potentiate sonodynamic therapy via reshaping tumor microenvironment and facilitating electron-hole pairs' separation, *Adv. Funct. Mater.* 30 (2020).
- [19] Y. Yin, X. Jiang, L. Sun, H. Li, C. Su, Y. Zhang, G. Xu, X. Li, C. Zhao, Y. Chen, H. Xu, K. Zhang, Continuous inertial cavitation evokes massive ROS for reinforcing sonodynamic therapy and immunogenic cell death against breast carcinoma, *Nano Today* 36 (2021).
- [20] Y. Cheng, H. Cheng, C. Jiang, X. Qiu, K. Wang, W. Huan, A. Yuan, J. Wu, Y. Hu, Perfluorocarbon nanoparticles enhance reactive oxygen levels and tumour growth inhibition in photodynamic therapy, *Nat. Commun.* 6 (2015).
- [21] X. Song, L. Feng, C. Liang, K. Yang, Z. Liu, Ultrasound triggered tumor oxygenation with oxygen-shuttle nanoperfluorocarbon to overcome hypoxia-associated resistance in cancer therapies, *Nano Lett* 16 (2016) 6145–6153.
- [22] Q. Chen, L. Feng, J. Liu, W. Zhu, Z. Dong, Y. Wu, Z. Liu, Intelligent albumin-MnO₂ nanoparticles as pH-/H₂O₂-responsive dissociable nanocarriers to modulate tumor hypoxia for effective combination therapy, *Adv. Mater.* 28 (2016) 7129–+.
- [23] W. Zhu, Z. Dong, T. Fu, J. Liu, Q. Chen, Y. Li, R. Zhu, L. Xu, Z. Liu, Modulation of hypoxia in solid tumor microenvironment with MnO₂ nanoparticles to enhance photodynamic therapy, *Adv. Funct. Mater.* 26 (2016) 5490–5498.
- [24] W. Xu, C. Dong, H. Hu, X. Qian, L. Chang, Q. Jiang, L. Yu, Y. Chen, J. Zhou, Engineering janus chemoreactive nanosensitizers for bilaterally augmented sonodynamic and chemodynamic cancer nanotherapy, *Adv. Funct. Mater.* 31 (2021).
- [25] K. Zhang, X. Meng, Z. Yang, H. Dong, X. Zhang, Enhanced cancer therapy by hypoxia-responsive copper metal-organic frameworks nanosystem, *Biomaterials* 258 (2020).
- [26] S. Liang, X. Deng, G. Xu, X. Xiao, M. Wang, X. Guo, P.a. Ma, Z. Cheng, D. Zhang, J. Lin, A novel Pt-TiO₂ heterostructure with oxygen-deficient layer as bilaterally enhanced sonosensitizer for synergistic chemo-sonodynamic cancer therapy, *Adv. Funct. Mater.* 30 (2020).
- [27] D. Sun, X. Pang, Y. Cheng, J. Ming, S. Xiang, C. Zhang, P. Lv, C. Chu, X. Chen, G. Liu, N. Zheng, Ultrasound-switchable nanozyme augments sonodynamic therapy against multidrug-resistant bacterial infection, *ACS Nano* 14 (2020) 2063–2076.
- [28] Z. Wang, B. Liu, Q. Sun, L. Feng, F. He, P. Yang, S. Gai, Z. Quan, J. Lin, Upconverted metal-organic framework janus architecture for near-infrared and ultrasound Co-enhanced high performance tumor therapy, *ACS Nano* 15 (2021) 12342–12357.
- [29] T. Zhang, Y. Sun, J. Cao, J. Luo, J. Wang, Z. Jiang, P. Huang, Intrinsic nucleus-targeted ultra-small metal-organic framework for the type I sonodynamic treatment of orthotopic pancreatic carcinoma, *J. Nanobiotechnol.* 19 (2021).
- [30] L.-S. Lin, J. Song, L. Song, K. Ke, Y. Liu, Z. Zhou, Z. Shen, J. Li, Z. Yang, W. Tang, G. Niu, H.-H. Yang, X. Chen, Simultaneous fenton-like ion delivery and glutathione depletion by MnO₂-based nanoagent to enhance chemodynamic therapy, *Angew. Chem., Int. Ed.* 57 (2018) 4902–4906.
- [31] G. Feng, J. Liu, C.-J. Zhang, B. Liu, Artemisinin and ALEgen conjugate for mitochondria-targeted and image-guided chemo- and photodynamic cancer cell ablation, *ACS Appl. Mater. Interfaces* 10 (2018) 11546–11553.
- [32] Y. Luo, X. Sun, L. Huang, J. Yan, B.-Y. Yu, J. Tian, Artemisinin-based smart nanomedicines with self-supply of ferrous ion to enhance oxidative stress for specific and efficient cancer treatment, *ACS Appl. Mater. Interfaces* 11 (2019) 29490–29497.
- [33] X. Wan, H. Zhong, W. Pan, Y. Li, Y. Chen, N. Li, B. Tang, Programmed release of dihydroartemisinin for synergistic cancer therapy using CaCO₃ mineralized metal-organic framework, *Angew. Chem., Int. Ed.* 58 (2019) 14134–14139.
- [34] G.Q. Chen, F.A. Benthani, J. Wu, D.G. Liang, Z.X. Bian, X.J. Jiang, Artemisinin compounds sensitize cancer cells to ferroptosis by regulating iron homeostasis, *Cell Death Differ* 27 (2020) 242–254.
- [35] F. Gao, Z. Sun, F.G. Kong, J.Q. Xiao, Artemisinin-derived hybrids and their anticancer activity, *Eur. J. Med. Chem.* 188 (2020) 14.
- [36] X. Sun, P. Yan, C. Zou, Y.-K. Wong, Y. Shu, Y.M. Lee, C. Zhang, N.-D. Yang, J. Wang, J. Zhang, Targeting autophagy enhances the anticancer effect of artemisinin and its derivatives, *Med. Res. Rev.* 39 (2019) 2172–2193.
- [37] J.G. Wang, C.C. Xu, Y.K. Wong, Y.J. Li, F.L. Liao, T.L. Jiang, Y.Y. Tu, Artemisinin, the magic drug discovered from traditional Chinese medicine, *Engineering* 5 (2019) 32–39.
- [38] Y.X. Ding, J.X. Wan, Z.H. Zhang, F. Wang, J. Guo, C.C. Wang, Localized Fe(II)-Induced cytotoxic reactive oxygen species generating nanosystem for enhanced anticancer therapy, *ACS Appl. Mater. Interfaces* 10 (2018) 4439–4449.
- [39] W.E. Ho, H.Y. Peh, T.K. Chan, W.S.F. Wong, Artemisinins: pharmacological actions beyond anti-malarial, *Pharmacol. Ther.* 142 (2014) 126–139.
- [40] T. Efferth, From ancient herb to modern drug: Artemisia annua and artemisinin for cancer therapy, *Semin. Cancer Biol.* 46 (2017) 65–83.
- [41] H.J. Chen, X.R. Huang, X.B. Zhou, B.Y. Zheng, J.-D. Huang, Potential sonodynamic anticancer activities of artemether and liposome-encapsulated artemether, *Chem. Commun.* 51 (2015) 4681–4684.
- [42] L. Wang, Y. Hu, Y. Hao, L. Li, C. Zheng, H. Zhao, M. Niu, Y. Yin, Z. Zhang, Y. Zhang, Tumor-targeting core-shell structured nanoparticles for drug procedural controlled release and cancer sonodynamic combined therapy, *J. Controlled Release* 286 (2018) 74–84.
- [43] S. Gao, X.H. Cheng, J.H. Li, Lipid nanobubbles as an ultrasound-triggered artesunate delivery system for imaging-guided, tumor-targeted chemotherapy, *OncoTargets Ther* 12 (2019) 1841–1850.
- [44] K. Tiensomjit, S. Prabpai, P. Kongsaeer, Characterization of the selective alkylation site in hemoglobin A by dihydroartemisinin with tandem mass spectrometry, *Int. J. Biol. Macromol.* 99 (2017) 358–364.
- [45] J. Jourdan, A. Walz, H. Matile, A. Schmidt, J.B. Wu, X.F. Wang, Y.X. Dong, J. L. Vennerstrom, R.S. Schmidt, S. Wittlin, P. Maser, Stochastic protein alkylation by antimalarial peroxides, *ACS Infect. Dis.* 5 (2019) 2067–2075.
- [46] Z.G. Chen, X.X. Kang, Y.X. Wu, H.H. Xiao, X.Z. Cai, S.H. Sheng, X.F. Wang, S. G. Chen, A mitochondria targeting artesunate prodrug-loaded nanoparticle exerting anticancer activity via iron-mediated generation of the reactive oxygen species, *Chem. Commun.* 55 (2019) 4781–4784.
- [47] X.F. Tang, W.X. Tang, Z. Yang, X.G. Luo, H.Y. Luo, D. Gao, Y. Chen, Q. Jiang, J. Liu, Z.Z. Jiang, PEGylated poly(amine-co-ester) micelles as biodegradable non-viral gene vectors with enhanced stability, reduced toxicity and higher in vivo transfection efficacy, *J. Mater. Chem. B* 2 (2014) 4034–4044.
- [48] Y.H. Gong, M. Shu, J.H. Xie, C. Zhang, Z. Cao, Z.Z. Jiang, J. Liu, Enzymatic synthesis of PEG-poly(amine-co-thioether esters) as highly efficient pH and ROS dual-responsive nanocarriers for anticancer drug delivery, *J. Mater. Chem. B* 7 (2019) 651–664.
- [49] H.L. Li, J.M. Li, X.Y. He, B. Zhang, C.X. Liu, Q.F. Li, Y. Zhu, W.L. Huang, W. Zhang, H. Qian, L. Ge, Histology and antitumor activity study of PTX-loaded micelle, a fluorescent drug delivery system prepared by PEG-TTPP, *Chin. Chem. Lett.* 30 (2019) 1083–1088.
- [50] W. Yu, M. Shevtsov, X. Chen, H. Gao, Advances in aggregatable nanoparticles for tumor-targeted drug delivery, *Chin. Chem. Lett.* 31 (2020) 1366–1374.
- [51] M. Liu, H. Du, A.R. Khan, J. Ji, A. Yu, G. Zhai, Redox/enzyme sensitive chondroitin sulfate-based self-assembled nanoparticles loading docetaxel for the inhibition of metastasis and growth of melanoma, *Carbohydr. Polym.* 184 (2018) 82–93.
- [52] M. Liu, H. Du, W. Zhang, G. Zhai, Internal stimuli-responsive nanocarriers for drug delivery: design strategies and applications, *Mater. Sci. Eng., C* 71 (2017) 1267–1280.
- [53] Y. Liu, W. Zhen, Y. Wang, J. Liu, L. Jin, T. Zhang, S. Zhang, Y. Zhao, S. Song, C. Li, J. Zhu, Y. Yang, H. Zhang, One-dimensional Fe₂P acts as a fenton agent in response to NIR II light and ultrasound for deep tumor synergetic theranostics, *Angew. Chem., Int. Ed.* 58 (2019) 2407–2412.

- [54] H. Wu, D. Gu, S. Xia, F. Chen, C. You, B. Sun, One-for-all intelligent core-shell nanoparticles for tumor-specific photothermal-chemodynamic synergistic therapy, *Biomater. Sci.* 9 (2021) 1020–1033.
- [55] D.D. Wang, J.J. Zhou, R.H. Chen, R.H. Ship, C.L. Wang, J. Lu, G.Z. Zhao, G.L. Xia, S. Zhou, Z.B. Liu, H.B. Wang, Z. Guo, Q.W. Chen, Core-shell metal-organic frameworks as Fe²⁺ suppliers for Fe²⁺-mediated cancer therapy under multimodality imaging, *Chem. Mater.* 29 (2017) 3477–3489.
- [56] D. Wang, J. Zhou, R. Chen, R. Shi, G. Zhao, G. Xia, R. Li, Z. Liu, J. Tian, H. Wang, Z. Guo, H. Wang, Q. Chen, Controllable synthesis of dual-MOFs nanostructures for pH-responsive artemisinin delivery, magnetic resonance and optical dual-modal imaging-guided chemo/photothermal combinational cancer therapy, *Biomaterials* 100 (2016) 27–40.
- [57] R.Y. Lin, Z.H. Zhang, L.F. Chen, Y.F. Zhou, P. Zou, C. Feng, L. Wang, G. Liang, Dihydroartemisinin (DHA) induces ferroptosis and causes cell cycle arrest in head and neck carcinoma cells, *Cancer Lett* 381 (2016) 165–175.